

IMEX large time step finite volume methods for low Froude number shallow water flows

G. Bispen*, K.R. Arun†, M. Lukáčová-Medvidová*, and S. Noelle‡

Abstract

We present new large time step methods for the shallow water flows in the low Froude number limit. In order to take into account multiscale phenomena that typically appear in geophysical flows nonlinear fluxes are split into a linear part governing the gravitational waves and the nonlinear advection. We propose to approximate fast linear waves implicitly in time and in space by means of a genuinely multidimensional evolution operator. On the other hand, we approximate nonlinear advection part explicitly in time and in space by means of the method of characteristics or some standard numerical flux function. Time integration is realized by the implicit-explicit (IMEX) method. We apply the IMEX Euler scheme, two step Runge Kutta Crank Nicolson scheme, as well as the semi-implicit BDF scheme and prove their asymptotic preserving property in the low Froude number limit. Numerical experiments demonstrate stability, accuracy and robustness of these new large time step finite volume schemes with respect to small Froude number.

Key words: low Froude number flows, asymptotic preserving schemes, shallow water equations, large time step, semi-implicit approximation, evolution Galerkin schemes

AMS Subject Classification: 35L65, 76B15, 65M08, 65M06, 35L45, 35L65

1 Introduction

In oceanography, meteorology or river flow engineering shallow water models are used to describe a thin layer of constant density fluid in hydrostatic balance bounded from below by a rigid surface, see, e.g., [8, 11, 22, 45]. The shallow water equations (SWE)

$$\begin{bmatrix} h \\ hu \\ hv \end{bmatrix}_t + \begin{bmatrix} hu \\ hu^2 + \frac{1}{2\varepsilon^2}h^2 \\ huv \end{bmatrix}_x + \begin{bmatrix} hv \\ huv \\ hv^2 + \frac{1}{2\varepsilon^2}h^2 \end{bmatrix}_y = \begin{bmatrix} 0 \\ -\frac{1}{\varepsilon^2}h\tilde{b}_x \\ -\frac{1}{\varepsilon^2}h\tilde{b}_y \end{bmatrix} \quad (1)$$

*Institute of Mathematics, University of Mainz, Germany; {bispeng, lukacova}@uni-mainz.de

†School of Mathematics, Indian Institute of Science Education and Research Thiruvananthapuram, India; arun@iisertvm.ac.in

‡IGPM, RWTH Aachen, Germany; noelle@igpm.rwth-aachen.de

describe the motion of shallow water, where h is the water depth, $\mathbf{u} = (u, v)$; u, v are the velocities in x - and y -direction and \tilde{b} is time independent bottom topography. Further, $\varepsilon := u_{ref}/c_{ref} = u_{ref}/\sqrt{gh_{ref}}$ is the reference Froude number, g is the gravitational constant, u_{ref} and h_{ref} are the problem dependent reference values for velocity and water depth, respectively. System (1) is a hyperbolic balance law, which can be derived by integrating the Navier-Stokes equations along the vertical axis [45].

Let us note that geophysical flows are typically perturbations of some underlying equilibrium state. One possibility to take the loss of significance into account is to approximate just the perturbation of the equilibrium states [15, 34]. For the shallow water equations (1) the so-called lake at rest solution $h + b = \text{const.}$, $u = 0 = v$ is the equilibrium state.

We would like to point out, that in literature there are already several approaches that describe how to design a numerical scheme which satisfies some important equilibrium conditions, such as the lake at rest state or the geostrophic equilibrium, exactly for given discrete data. Such schemes are called *well-balanced schemes* or schemes satisfying the so-called *C-property*, we refer a reader to, e.g., [4, 7, 10, 16, 24, 25, 26, 27, 32] and to [5], where the C-property has been introduced firstly. We will discuss the question of well-balancing more deeply in Sections 4.3 and 5 and show that our newly developed large time step schemes are well-balanced for the lake at rest uniformly with respect to the Froude number ε .

Now, we introduce the following variable transformation $w = (z, m, n) := (h + b, hu, hv)$. Here z is the perturbation of the constant water level $H = h + \tilde{b}$ and $b = \tilde{b} - RBC < 0$ with a problem defined relative bottom topography constant RBC . We should also note that an analogous variable transformation has been already used in [26], [27], [24], [41] and [42]. The only difference in our case is that we introduce explicitly a “shift” of the coordinate system in the vertical direction by a suitable constant denoted by RBC in order to obtain a still water level to be zero. Consequently, we aim to have the perturbation z to be a small positive or negative value. Note that by this transformation we obtain bottom topography function $b < 0$. System (1) can be now rewritten in the non-dimensional form using the new variables z, m, n

$$\begin{bmatrix} z \\ m \\ n \end{bmatrix}_t + \begin{bmatrix} \frac{m^2}{z-b} + \frac{1}{2\varepsilon^2}z^2 - \frac{1}{\varepsilon^2}zb \\ \frac{mn}{z-b} \end{bmatrix}_x + \begin{bmatrix} \frac{n^2}{z-b} + \frac{1}{2\varepsilon^2}z^2 - \frac{1}{\varepsilon^2}zb \end{bmatrix}_y = \begin{bmatrix} 0 \\ -\frac{1}{\varepsilon^2}zb_x \\ -\frac{1}{\varepsilon^2}zb_y \end{bmatrix}. \quad (2)$$

In geophysical problems *low Froude number shallow water flows* typically appear, cf. [22], [33], [45]. This means that the advection speed u_{ref} is much smaller than the speed of gravitational waves c_{ref} and thus $\varepsilon \ll 1$. Indeed, as stated in [33] the shallow water theory is an appropriate approximation for atmospheric and oceanic motions in the midlatitudes with relatively large length and time scales. For example, in the atmosphere typical scales of motion include wind speeds $u_{ref} = 10 \text{ ms}^{-1}$ and the vertical length scales $h_{ref} = 10 \text{ km}$; consequently the reference Froude number $\varepsilon = u_{ref}/\sqrt{gh_{ref}} = 0.03$. Similarly, the current velocity in oceans is approximately $u_{ref} = 1 \text{ ms}^{-1}$ and the vertical length depth h_{ref} is around 100 m. Therefore for the oceanic current motions we have again the Froude number ε around 0.03. Consequently, we have in (2) terms of different ε -like orders. If time explicit discretization is used in (2) then the Froude number dictates the time steps

via the following CFL condition

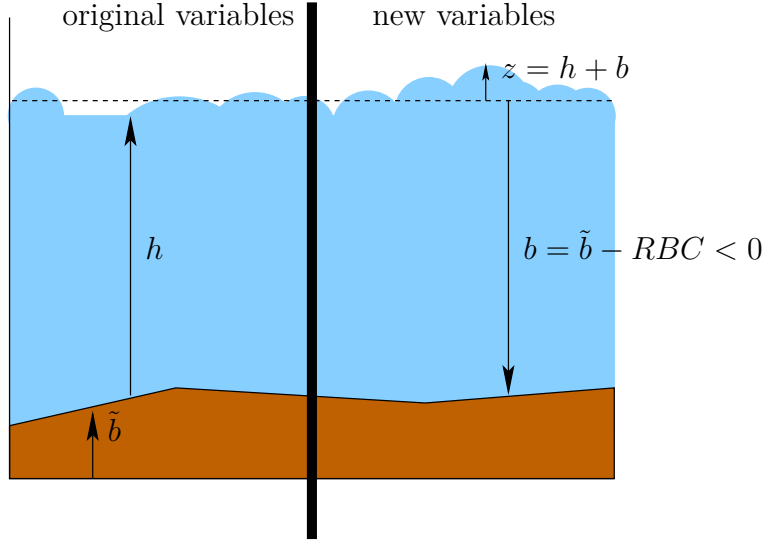
$$\max\left(\frac{|u|+c}{\Delta x}, \frac{|v|+c}{\Delta y}\right) \Delta t \approx \left(1 + \frac{1}{\varepsilon}\right) \max\left(\frac{|u|}{\Delta x}, \frac{|v|}{\Delta y}\right) \Delta t = CFL \leq 1. \quad (3)$$

In order to overcome a strong stability limitation of explicit schemes several split-explicit, implicit or semi-implicit schemes have been proposed in the literature, cf. [6, 14, 15, 21, 23, 34, 35, 38, 39]. In the case of semi-implicit schemes slow waves are typically approximated explicitly and fast implicitly in time. Since the problem is fully nonlinear, the crucial question is how to split the governing equations into subsystems modelling slow/fast waves. There are various methods, more or less efficient, that have been proposed in the literature; see, e.g. [18, 14, 15, 21, 34, 36, 38, 39], as well as [3, 2, 30] for recent results.

The aim of this paper is to derive and analyse a new large time step finite volume scheme for the shallow water equations. We use implicit-explicit (IMEX) time discretization and split the shallow water equations (2) into a linear system describing the gravitational waves and a nonlinear advection part. The novelty of our approach is to approximate the fast gravitational waves in a multidimensional way. Indeed, we approximate the gravitational waves implicitly in time and in space by means of a multidimensional evolution operator that takes all infinitely many directions of wave propagation into account. Nonlinear advection will be approximated explicitly in time and in space by means of a characteristic scheme or by using some standard flux-vector splitting scheme. We will derive first and second order large time step finite volume schemes and analyze them from the viewpoint of accuracy and asymptotic behaviour with respect to ε . In order to preserve the lake at rest steady state we will approximate the source term in a suitable way. Further, we analyze the underlying elliptic eigenvalue problem that results from our linear/nonlinear splitting approach and prove that our large time step schemes are indeed well-balanced uniformly with respect to $\varepsilon > 0$.

The paper is organized as follows. In the next section suitable IMEX time discretizations for the first and second order methods are proposed. Next, in Section 3 we will derive exact integral representation and approximate evolution operators for both, the linear operator describing the gravitational waves, as well as the nonlinear operator for the advection. We will also prove that the proposed IMEX-type time discretization are the so-called asymptotically stable, i.e. the approximation is stable with respect to the small parameter ε . Further, in Section 4 we derive the large time step finite volume scheme using the above IMEX-type time discretization and the finite volume spatial discretization. As a predictor step to evaluate cell interface fluxes, the approximate evolution operators will be used. In Section 5 behaviour of the proposed large time step finite volume schemes will be illustrated on a series of numerical experiments. Numerical experiments demonstrate high accuracy as well as asymptotic preserving properties of new large time step finite volume schemes.

Figure 1: Variable transformation for the shallow water equations.



2 Time discretization

The aim of this section is to propose suitable time discretizations that efficiently resolve multiscale behaviour of the solution of the shallow water equations (2). We follow Restelli et al. [14, 38] and split the full nonlinear flux and the source term from (2) into a linear part governing the gravitational waves and the nonlinear part that models advection flow. Let us note that we will obtain in this way a splitting into stiff and nonstiff parts. More precisely, we can rewrite (2), i.e.

$$w_t = \mathcal{N}(w)$$

as follows

$$w_t = \mathcal{L}(w) + (\mathcal{N} - \mathcal{L})(w), \quad (4)$$

where

$$\begin{aligned} \mathcal{L}(w) &= -\nabla \cdot \mathcal{F}_L(w) + K(w) \quad \text{with} \\ \mathcal{F}_L(w) &= \begin{bmatrix} m & n \\ \frac{-b}{\varepsilon^2} z & 0 \\ 0 & \frac{-b}{\varepsilon^2} z \end{bmatrix}, \quad K = \begin{bmatrix} 0 \\ -\frac{zb_x}{\varepsilon^2} \\ -\frac{zb_y}{\varepsilon^2} \end{bmatrix} \end{aligned} \quad (5)$$

and

$$\begin{aligned} (\mathcal{N} - \mathcal{L})(w) &= -\nabla \cdot \mathcal{F}_{NL}(w) \quad \text{with} \\ \mathcal{F}_{NL}(w) &= \begin{bmatrix} 0 & 0 \\ \frac{m^2}{z-b} + \frac{1}{2\varepsilon^2} z^2 & \frac{mn}{z-b} \\ \frac{mn}{z-b} & \frac{n^2}{z-b} + \frac{1}{2\varepsilon^2} z^2 \end{bmatrix}. \end{aligned} \quad (6)$$

We would like to point out that the choice of the linear operator \mathcal{L} is a crucial step. Indeed, it is the operator that has to model gravitational waves.

In order to relax the strong stability condition (3), we now approximate the linear operator \mathcal{L} implicitly in time, whereas the nonlinear operator $\mathcal{N} - \mathcal{L}$ will be approximated explicitly. Consequently, we will use only the advection velocity as the restriction for time step Δt through the following CFL stability condition

$$\max\left(\frac{|u|}{\Delta x}, \frac{|v|}{\Delta y}\right) \Delta t = CFL_u \leq 1. \quad (7)$$

In what follows we present three IMEX-type time discretizations of (2) and show that they satisfy the so-called asymptotic preserving property, cf. [19].

The first order approximation is obtained by integrating (2) from t^n to t^{n+1} and approximating the flux integrals by the rectangle rule - implicitly for the linear part and explicitly for the nonlinear one, yielding

$$w^{n+1} = w^n - \Delta t \nabla \cdot [\mathcal{F}_L(w^{n+1}) + \mathcal{F}_{NL}(w^n)] + \Delta t K(w^{n+1}). \quad (8)$$

Let us point out that since the source is stiff it is treated implicitly. The local truncation error of this time discretization is of the second order. To obtain the third order local truncation error we predict solution $w^{n+\frac{1}{2}}$ at half time step with scheme (8) and then use the midpoint rule for the nonlinear part and the trapezoidal rule for the linear one. This yields us the so-called second order Runge-Kutta Cranck Nicolson (RK2CN) scheme

$$\begin{aligned} w^{n+\frac{1}{2}} &= w^n - \frac{\Delta t}{2} \nabla \cdot \mathcal{F}_{NL}(w^n) - \frac{\Delta t}{2} \nabla \cdot \mathcal{F}_L(w^{n+\frac{1}{2}}) + \frac{\Delta t}{2} K(w^{n+\frac{1}{2}}) \\ w^{n+1} &= w^n - \Delta t \nabla \cdot \mathcal{F}_{NL}(w^{n+\frac{1}{2}}) - \frac{\Delta t}{2} \nabla \cdot [\mathcal{F}_L(w^n) + \mathcal{F}_L(w^{n+1})] + \frac{\Delta t}{2} [K(w^n) + K(w^{n+1})], \end{aligned} \quad (9)$$

see also [36] for another use of RK2CN for low Mach number problems. The third time approximation scheme is obtained by applying the backward difference method to approximate the time derivative

$$\frac{w^{n+1} - \alpha_0 w^n - \alpha_1 w^{n-1}}{-\beta} \approx w_t^{n+1} = -\nabla \cdot \mathcal{F}_L(w^{n+1}) - \nabla \cdot \mathcal{F}_{NL}(w^{n+1}) + K(w^{n+1}). \quad (10)$$

This yields the fully implicit scheme

$$\begin{aligned} w^{n+1} &= \alpha_0 w^n + \alpha_1 w^{n-1} \\ &+ \beta \left\{ \nabla \cdot \mathcal{F}_L(w^{n+1}) + \nabla \cdot \mathcal{F}_{NL}(w^{n+1}) - K(w^{n+1}) \right\} \end{aligned} \quad (11)$$

with $\alpha_0, \alpha_1, \beta$ coefficients resulting from the corresponding Taylor expansion, see Table 1.

α_0	α_1	β	β_0	β_1	$\tilde{\beta}_0$	$\tilde{\beta}_1$
$\frac{(a+c)^2}{c(2a+c)}$	$-\frac{a^2}{c(2a+c)}$	$-\frac{a(a+c)}{2a+c}$	$-\frac{a(a+c)^2}{c(2a+c)}$	$\frac{a^2(a+c)}{c(2a+c)}$	a	$-\frac{a^2}{2a+c}$

Table 1: Coefficients of the backward difference method for non-constant times steps $a = t^{n+1} - t^n, c = t^n - t^{n-1}$.

In the case of equidistant time steps, this discretization reduces to the standard BDF2 method, cf. [15, 38]. Since we want to solve the nonlinear flux explicitly, we further approximate $\mathcal{F}_{NL}(w^{n+1})$ by a linear interpolation, obtaining

$$\begin{aligned}
w^{n+1} &= \alpha_0 w^n + \alpha_1 w^{n-1} \\
&+ \nabla \cdot \left\{ \beta \mathcal{F}_L(w^{n+1}) + \beta_0 \mathcal{F}_{NL}(w^n) + \beta_1 \mathcal{F}_{NL}(w^{n-1}) \right\} \\
&- \beta K(w^{n+1}).
\end{aligned} \tag{12}$$

Alternatively, interpolating the nonlinear part of the flux at $t^{n-\frac{1}{2}}, t^{n+\frac{1}{2}}$ leads to

$$\begin{aligned}
w^{n+1} &= \alpha_0 w^n + \alpha_1 w^{n-1} \\
&+ \nabla \cdot \left\{ \beta \mathcal{F}_L(w^{n+1}) + \tilde{\beta}_0 \mathcal{F}_{NL}(w^{n+\frac{1}{2}}) + \tilde{\beta}_1 \mathcal{F}_{NL}(w^{n-\frac{1}{2}}) \right\} \\
&- \beta K(w^{n+1}).
\end{aligned} \tag{13}$$

As we will see in the next section the implicit time approximation of the source term in all cases is necessary for the method to satisfy the asymptotic preserving property.

2.1 Asymptotic preserving property

The aim of this section is to show the asymptotic preserving property of the time discretizations (8), (9), (12) and (13). To this end, let us consider a general singular perturbation problem \mathcal{P}^ε and suppose that its solution converges to the solution of a limit problem \mathcal{P}^0 as $\varepsilon \rightarrow 0$. A scheme $\mathcal{P}^{\varepsilon, h}$ with a discretization parameter h is called *asymptotic preserving (AP)*, if its limit, say $\mathcal{P}^{0, h}$, is a consistent approximation of the problem \mathcal{P}^0 and a stability constraint on h is independent of ε .

The asymptotic limit of the shallow water equations (1) can be investigated by the procedure of Klainerman and Majda [20]. This means that we consider formally the asymptotic expansion

$$f(x) = f^{(0)}(x) + \varepsilon f^{(1)}(x) + \varepsilon^2 f^{(2)}(x) \tag{14}$$

for the unknown functions h, u, v . We plug in this expansion to the nondimensional form of the equation (1) and collect the like powers of ε :

$$\varepsilon^2 : \quad h^{(0)} \nabla h^{(0)} = -h^{(0)} \nabla b \tag{15}$$

$$\varepsilon^1 : \quad h^{(0)} \nabla h^{(1)} + h^{(1)} \nabla h^{(0)} = -h^{(1)} \nabla b \tag{16}$$

$$\varepsilon^0 : \quad h_t^{(0)} + \nabla \cdot (h^{(0)} \mathbf{u}^{(0)}) = 0 \tag{17}$$

$$(h^{(0)} \mathbf{u}^{(0)})_t + \nabla \cdot (h^{(0)} \mathbf{u}^{(0)} \otimes \mathbf{u}^{(0)}) + (h \nabla h)^{(2)} = -h^{(2)} \nabla b. \tag{18}$$

Obviously, we first have

$$h^{(0)} + b =: z^{(0)}(t), \quad h^{(1)} = h^{(1)}(t), \quad h_t^{(0)} + \nabla \cdot (h^{(0)} \mathbf{u}^{(0)}) = 0. \quad (19)$$

We average (19) over the entire flow domain Ω and obtain by the Gauss theorem

$$-\frac{dz^{(0)}}{dt} = -\frac{dh^{(0)}}{dt} = \frac{1}{|\Omega|} \int_{\partial\Omega} h^{(0)} \mathbf{u}^{(0)} \cdot \mathbf{n} \, ds. \quad (20)$$

Consequently, the limit equations read

$$\begin{aligned} h^{(0)} + b &= z^{(0)}(t) \\ \nabla \cdot (h^{(0)} \mathbf{u}^{(0)}) &= -\frac{dz^{(0)}}{dt} = \frac{1}{|\Omega|} \int_{\partial\Omega} h^{(0)} \mathbf{u}^{(0)} \cdot \mathbf{n} \, ds \\ (h^{(0)} \mathbf{u}^{(0)})_t + \nabla \cdot (h^{(0)} \mathbf{u}^{(0)} \otimes \mathbf{u}^{(0)}) + h^{(0)} \nabla h^{(2)} &= 0. \end{aligned} \quad (21)$$

Then by (19) $z^{(0)}$ as well as $h^{(1)}$ are constant in space. Further, the integral over the entire domain in (20) vanishes for certain boundary conditions, e.g. periodic boundary conditions, slip boundary conditions or under the sublinear growth condition for $\mathbf{u}^{(0)}$ and $h^{(0)}$

$$\mathbf{u}^{(0)}(x), h^{(0)}(x) = o(|x|), \quad x \rightarrow \infty, \quad (22)$$

cf. [9], [17]. Then (21) yields for constant bottom topography the limit equations in the following form

$$\begin{aligned} h^{(0)} &= \text{const.} \\ \nabla \cdot \mathbf{u}^{(0)} &= 0 \\ \mathbf{u}_t^{(0)} + \nabla \cdot (\mathbf{u}^{(0)} \otimes \mathbf{u}^{(0)}) + \nabla h^{(2)} &= 0. \end{aligned} \quad (23)$$

Rewriting (21) using the variables (z, m, n) , $\mathbf{m} = (m, n)$, we obtain the following limit equations

$$z^{(0)} \equiv Z = \text{const.} \quad (24)$$

$$\nabla \cdot \mathbf{m}^{(0)} = 0 \quad (25)$$

$$\mathbf{m}_t^{(0)} + \frac{1}{Z-b} \nabla \cdot (\mathbf{m}^{(0)} \otimes \mathbf{m}^{(0)}) + (Z-b) \nabla z^{(2)} = 0. \quad (26)$$

In the next subsection we will show that the IMEX-type discretizations (8), (9), (12) and (13) are asymptotic preserving, i.e. in the limit as $\varepsilon \rightarrow 0$ they yield a consistent approximation of the above limiting equations (24), (25) and (26).

2.1.1 AP Property of the IMEX-type time discretizations

In this section we will prove the AP property of the IMEX-type time discretization schemes introduced above. Let us firstly assume well-prepared data of the following form

$$\begin{aligned} z^n(x) &= z^{(0),n} + \varepsilon z^{(1),n} + \varepsilon^2 z^{(2),n}(x), \\ \mathbf{m}^n(x) &= \mathbf{m}^{(0),n}(x) + \varepsilon \mathbf{m}^{(1),n}(x) + \varepsilon^2 \mathbf{m}^{(2),n}(x), \\ z^{n-1}(x) &= z^{(0),n-1} + \varepsilon z^{(1),n-1} + \varepsilon^2 z^{(2),n-1}(x), \\ \mathbf{m}^{n-1}(x) &= \mathbf{m}^{(0),n-1}(x) + \varepsilon \mathbf{m}^{(1),n-1}(x) + \varepsilon^2 \mathbf{m}^{(2),n-1}(x). \end{aligned} \quad (27)$$

We now insert the expansions (27) into the scheme (12) and collect the like powers of ε . The terms with ε^{-1} , ε^{-2} give formally

$$\nabla z^{(0),n+1} = \nabla z^{(1),n+1} = 0. \quad (28)$$

Further the leading order terms in ε give

$$z^{(0),n+1} = \alpha_0 z^{(0),n} + \alpha_1 z^{(0),n-1} + \beta \nabla \cdot \mathbf{m}^{(0),n+1} \quad (29)$$

$$\begin{aligned} \mathbf{m}^{(0),n+1} &= \alpha_0 \mathbf{m}^{(0),n} + \alpha_1 \mathbf{m}^{(0),n-1} - \beta b \nabla z^{(2),n+1} \\ &+ \beta_0 \left[\frac{\nabla \cdot (\mathbf{m}^{(0),n} \otimes \mathbf{m}^{(0),n})}{z^{(0),n} - b} + z^{(0),n} \nabla z^{(2),n} \right] \\ &+ \beta_1 \left[\frac{\nabla \cdot (\mathbf{m}^{(0),n-1} \otimes \mathbf{m}^{(0),n-1})}{z^{(0),n-1} - b} + z^{(0),n-1} \nabla z^{(2),n-1} \right]. \end{aligned} \quad (30)$$

The equation (29) can be rewritten in the following way

$$\nabla \cdot \mathbf{m}^{(0),n+1} = \frac{z^{(0),n+1} - \alpha_0 z^{(0),n} - \alpha_1 z^{(0),n-1}}{\beta} = -z_t^{(0),n+1} + \mathcal{O}(\Delta t^2). \quad (31)$$

We use now the same argument as in the continuous case and integrate (31) over the computational domain to obtain that $\mathbf{m}^{(0),n+1}$ is divergence free using the sublinear growth condition (22) or the suitable boundary conditions, such as periodic boundary conditions, slip boundary conditions. Hence $z^{(0),n+1} = \text{const.} \equiv Z$.

For scheme (9) the proof is similar. We insert the asymptotic expansions (14) in the time discretization (9) and obtain formally that

$$\nabla z^{(0),n+1} = \nabla z^{(1),n+1} = 0.$$

Then we obtain $z^{(0),n+1} = z^{(0),n} = Z$ and $\mathbf{m}^{(0),n+1}$ to be divergence free from the equation for z

$$\nabla \cdot \mathbf{m}^{(0),n+1} = -2 \frac{z^{(0),n+1} - z^{(0),n}}{\Delta t} + z_t^{(0),n} = -z_t^{(0),n+1} + \mathcal{O}(\Delta t).$$

The limit of the momentum equation reads

$$\begin{aligned} \mathbf{m}^{(0),n+1} &= \mathbf{m}^{(0),n} - \frac{\Delta t}{2} b \nabla \left[z^{(2),n+1} + z^{(2),n} \right] \\ &+ \Delta t \left[\frac{\nabla \cdot (\mathbf{m}^{(0),n+\frac{1}{2}} \otimes \mathbf{m}^{(0),n+\frac{1}{2}})}{z^{(0),n+\frac{1}{2}} - b} + z^{(0),n+\frac{1}{2}} \nabla z^{(2),n+\frac{1}{2}} \right], \end{aligned}$$

which is a consistent approximation of (26).

The proof of the AP property for the time discretization schemes (12), (13) is analogous to that of the scheme (8). Summarizing the above results we have shown the following lemma.

Lemma 2.1 *The IMEX-type discretization schemes (8), (9), (12) and (13) are asymptotic preserving.*

3 Evolution operators

In the previous section we have proposed a suitable splitting of the whole shallow water equations (2) into the linear and nonlinear parts governing the gravitational waves and advection, respectively. Thus, using the operator splitting approach for (2) we will obtain the corresponding subsystems

$$w_t + \nabla \cdot \mathcal{F}_L(w) = K(w), \quad (32)$$

$$w_t + \nabla \cdot \mathcal{F}_{NL}(w) = 0. \quad (33)$$

Using the theory of bicharacteristics we will derive in this section exact and approximate evolution operators EG^L and EG^{NL} for (32) and (33), respectively. The approximate evolution operators are the main building blocks of the so-called evolution Galerkin schemes (FVEG), that have been studied extensively by Lukáčová, Noelle, Arun and collaborators. The main idea of the FVEG schemes is to apply the approximate evolution operators in order to predict a solution on cell interfaces and to evaluate cell interface fluxes. The later are used in the finite volume corrector step. Numerical results presented, e.g., in [1, 28, 29, 32], illustrate that the FVEG are approximating multidimensional flow phenomena in a very accurate and stable way. We refer a reader for more details to our review paper [31]. In what follows we will firstly derive exact integral representations of the subsystems (32) and (33) and then derive corresponding approximate evolution operators. These will be used later in Section 4 to formulate the finite volume update.

3.1 Evolution operator for the linear part

We will now derive the evolution operator for the linear part of the shallow water equations (32). Written in the quasilinear form $w_t + A_1 w_x + A_2 w_y = 0$, we have

$$\begin{bmatrix} z \\ m \\ n \end{bmatrix}_t + \begin{bmatrix} 0 & 1 & 0 \\ s^2 & 0 & 0 \\ 0 & 0 & 0 \end{bmatrix} \begin{bmatrix} z \\ m \\ n \end{bmatrix}_x + \begin{bmatrix} 0 & 0 & 1 \\ 0 & 0 & 0 \\ s^2 & 0 & 0 \end{bmatrix} \begin{bmatrix} z \\ m \\ n \end{bmatrix}_y = 0, \quad s = \frac{\sqrt{-b(x, y)}}{\varepsilon}. \quad (34)$$

The eigenvalues of the matrix pencil $P = A_1 \cos(\theta) + A_2 \sin(\theta)$, $\theta \in [0, 2\pi)$, are $\lambda_1 = -s$, $\lambda_2 = 0$, $\lambda_3 = s$. The matrix consisting of the right eigenvectors reads

$$R(\theta) = \begin{bmatrix} \frac{-1}{s} & 0 & \frac{1}{s} \\ \cos(\theta) & \sin(\theta) & \cos(\theta) \\ \sin(\theta) & -\cos(\theta) & \sin(\theta) \end{bmatrix}. \quad (35)$$

For $s \neq 0$, R is regular and the inverse matrix has the following form

$$R^{-1}(\theta) = \begin{bmatrix} \frac{-s}{2} & \frac{\cos(\theta)}{2} & \frac{\sin(\theta)}{2} \\ 0 & \sin(\theta) & -\cos(\theta) \\ \frac{s}{2} & \frac{\cos(\theta)}{2} & \frac{\sin(\theta)}{2} \end{bmatrix}. \quad (36)$$

Let $B_i = R^{-1}A_iR$ for $i = 1, 2$. Multiplying (34) by the matrix R^{-1} from the left and denoting $v := R^{-1}w$, the vector of characteristic variables, we get

$$v_t + B_1 v_x + B_2 v_y = ((R^{-1})_t + B_1 (R^{-1})_x + B_2 (R^{-1})_y)w =: F. \quad (37)$$

Here,

$$v = \begin{bmatrix} \frac{1}{2}[-zs + m \cos(\theta) + n \sin(\theta)] \\ m \sin(\theta) - n \cos(\theta) \\ \frac{1}{2}[zs + m \cos(\theta) + n \sin(\theta)] \end{bmatrix}. \quad (38)$$

This is equivalent to the quasi-diagonal form

$$v_t + D_1 v_x + D_2 v_y = ((R^{-1})_t + B_1(R^{-1})_x + B_2(R^{-1})_y)w - (B_1 - D_1)v_x - (B_2 - D_2)v_y =: F + S, \quad (39)$$

where D_i is the diagonal part of B_i and

$$B_1 = \begin{bmatrix} -s \cos \theta & -\frac{s}{2} \sin \theta & 0 \\ -s \sin \theta & 0 & s \sin \theta \\ 0 & \frac{s}{2} \sin \theta & s \cos \theta \end{bmatrix}, \quad B_2 = \begin{bmatrix} -s \sin \theta & \frac{s}{2} \cos \theta & 0 \\ s \cos \theta & 0 & -s \cos \theta \\ 0 & -\frac{s}{2} \cos \theta & s \sin \theta \end{bmatrix}. \quad (40)$$

Let us introduce the derivatives

$$D_\theta^+[f] := \cos(\theta) f_x + \sin(\theta) f_y \quad (41)$$

$$D_\theta^-[f] := \sin(\theta) f_x - \cos(\theta) f_y. \quad (42)$$

Each equation of the system (39) is valid along a corresponding family of bicharacteristic curves $\mathbf{x}^i = (x^i, y^i)$, $i = 1, 2, 3$. Time evolution of $\mathbf{x}^i(t)$ and the normal $\mathbf{n}(\theta^i(t)) = (\cos(\theta^i(t)), \sin(\theta^i(t)))$ can be obtained from the extended lemma on bicharacteristics, cf. [37]. This implies that

$$\frac{d\mathbf{x}^i}{dt}(t) = \nabla_{\mathbf{n}} \lambda_i(\mathbf{x}^i(t)), \quad i = 1, 2, 3,$$

where $\nabla_{\mathbf{n}} \lambda_i(\mathbf{x}^i(t))$ is the so-called ray velocity vector. Let us recall that the ray velocities are the velocities with which a point on the bicharacteristic moves in the (x, y) plane. More precisely, we can obtain the following system of ordinary differential equations

$$\begin{aligned} \frac{dx^1}{dt} &= -s(\mathbf{x}^1) \cos(\theta^1), & \frac{dy^1}{dt} &= -s(\mathbf{x}^1) \sin(\theta^1), & \frac{d\theta^1}{dt} &= -D_{\theta^1}^-[s](\mathbf{x}^1), \\ \frac{dx^2}{dt} &= 0, & \frac{dy^2}{dt} &= 0, & \frac{d\theta^2}{dt} &= 0, \\ \frac{dx^3}{dt} &= s(\mathbf{x}^3) \cos(\theta^3), & \frac{dy^3}{dt} &= s(\mathbf{x}^3) \sin(\theta^3), & \frac{d\theta^3}{dt} &= D_{\theta^3}^-[s](\mathbf{x}^3), \end{aligned} \quad (43)$$

where $\mathbf{x}^i(t^{n+1}) = (x_P, y_P)$, $\theta^i(t^{n+1}) = \omega$ and $P = (x_P, y_P, t^{n+1})$ is the apex of the bicharacteristic cone, $\omega \in [0, 2\pi)$.

Integrating each equation of (39) along the corresponding bicharacteristics from t^n to t^{n+1} implies

$$v_i^{n+1} = v_i^n(\mathbf{x}^i(t^n; \omega)) + \int_{t^n}^{t^{n+1}} \{F_i(\mathbf{x}^i(t; \omega), t) + S_i(\mathbf{x}^i(t; \omega), t)\} dt, \quad i = 1, 2, 3. \quad (44)$$

Now multiplying (44) by $R(\omega)$ and averaging over 0 to 2π we obtain after some lengthy calculations, see Appendix, the following exact integral representation:

$$(sz)(P) = \frac{1}{2\pi} \int_0^{2\pi} \{sz - m \cos \theta - n \sin \theta\} (\mathbf{x}^1(t^n; \omega), t^n) d\omega \\ - \frac{1}{2\pi} \int_0^{2\pi} \int_{t^n}^{t^{n+1}} \{sz D_\theta^+[s] + D_\theta^-[ms] \sin \theta - D_\theta^-[ns] \cos \theta\} (\mathbf{x}^1(t; \omega), t) dt d\omega, \quad (45)$$

$$m(P) = -\frac{1}{\pi} \int_0^{2\pi} \cos \omega \{sz - m \cos \theta - n \sin \theta\} (\mathbf{x}^1(t^n; \omega), t^n) d\omega \\ + \frac{1}{\pi} \int_0^{2\pi} \int_{t^n}^{t^{n+1}} \cos \omega \{sz D_\theta^+[s] + D_\theta^-[ms] \sin \theta - D_\theta^-[ns] \cos \theta\} (\mathbf{x}^1(t; \omega), t) dt d\omega, \quad (46)$$

$$n(P) = -\frac{1}{\pi} \int_0^{2\pi} \sin \omega \{sz - m \cos \theta - n \sin \theta\} (\mathbf{x}^1(t^n; \omega), t^n) d\omega \\ + \frac{1}{\pi} \int_0^{2\pi} \int_{t^n}^{t^{n+1}} \sin \omega \{sz D_\theta^+[s] + D_\theta^-[ms] \sin \theta - D_\theta^-[ns] \cos \theta\} (\mathbf{x}^1(t; \omega), t) dt d\omega, \quad (47)$$

$$\theta(\mathbf{x}^1(t; \omega), t) := \theta^1(t; \omega).$$

In what follows we will approximate (45)-(47) and derive a suitable approximate evolution operator. Denoting $\Delta t = t^{n+1} - t^n$, and applying the rectangle rule we approximate the bicharacteristic as follows

$$\mathbf{x}^1(t^n; \omega) = \mathbf{x}^1(t^{n+1}; \omega) + \int_{t^n}^{t^{n+1}} \begin{bmatrix} s \cos(\theta) \\ s \sin(\theta) \end{bmatrix} (\mathbf{x}^1(\tau; \omega), \tau) d\tau \quad (48) \\ = \begin{bmatrix} x_P \\ y_P \end{bmatrix} + \Delta t s(P) \begin{bmatrix} \cos(\omega) \\ \sin(\omega) \end{bmatrix} + \mathcal{O}(\Delta t^2).$$

Similarly,

$$\theta^1(t^n; \omega) = \theta^1(t^{n+1}; \omega) + \int_{t^n}^{t^{n+1}} D_\theta^-[s](\mathbf{x}^1(\tau; \omega), \tau) d\tau = \omega + \Delta t D_\omega^-[s](Q(t^n, \omega)) + \mathcal{O}(\Delta t^2). \quad (49)$$

This yields the approximations

$$\cos(\theta)(\mathbf{x}^1(t^n; \omega), t) = \cos(\omega) - \Delta t \sin(\omega) D_\omega^-[s](Q(t^n, \omega)) + \mathcal{O}(\Delta t^2) \quad (50) \\ \sin(\theta)(\mathbf{x}^1(t^n; \omega), t) = \sin(\omega) + \Delta t \cos(\omega) D_\omega^-[s](Q(t^n, \omega)) + \mathcal{O}(\Delta t^2).$$

Using first (48)-(50) and the rectangle rule in time at $t = t^n$, and then the product rule for the derivatives in the exact integral representation (45) yields

$$\begin{aligned}
(sz)(P) &= \frac{1}{2\pi} \int_0^{2\pi} \left\{ sz - m[\cos(\omega) - \Delta t \sin(\omega) D_\omega^-[s]] - n[\sin(\omega) + \Delta t \cos(\omega) D_\omega^-[s]] \right\} (Q(t^n, \omega)) d\omega \\
&\quad - \frac{\Delta t}{2\pi} \int_0^{2\pi} \left\{ sz D_\omega^+[s] + D_\omega^-[ms] \sin \omega - D_\omega^-[ns] \cos \omega \right\} (Q(t^n, \omega)) d\omega + \mathcal{O}(\Delta t^2) \\
&= \frac{1}{2\pi} \int_0^{2\pi} \left\{ sz - m \cos(\omega) - n \sin(\omega) \right\} (Q(t^n, \omega)) d\omega \\
&\quad - \frac{\Delta t}{2\pi} \int_0^{2\pi} \left\{ sz D_\omega^+[s] + D_\omega^-[m]s \sin \omega - D_\omega^-[n]s \cos \omega \right\} (Q(t^n, \omega)) d\omega + \mathcal{O}(\Delta t^2),
\end{aligned} \tag{51}$$

where

$$Q(t^n, \omega) := \begin{bmatrix} x_P \\ y_P \end{bmatrix} + \Delta t s(P) \begin{bmatrix} \cos(\omega) \\ \sin(\omega) \end{bmatrix}.$$

The expression for $m(P)$ and $n(P)$ are analogous. In [43] the so-called local evolution operator for the Euler equations has been derived by limiting $\Delta t \rightarrow 0$. Consequently, time integrals vanish in the limit. Repeating the procedure from [43], we can derive the local evolution operator also for the shallow water equations. Let us demonstrate the derivation for the equation (51).

To this end we need the following useful lemma, cf. [1, 43].

Lemma 3.1 *Let $f \in C^1(\mathbb{R}^2)$ and $p \in C^1(\mathbb{R})$. Partial integration leads to*

$$\begin{aligned}
&\int_\alpha^\beta p'(\omega) f(Q(t^n, \omega)) d\omega - p(\beta) f(Q(t^n, \beta)) + p(\alpha) f(Q(t^n, \alpha)) \\
&= \Delta t s(P) \int_\alpha^\beta p(\omega) D_\omega^-[f](Q(t^n, \omega)) d\omega, \quad (\alpha, \beta) \in [0, 2\pi].
\end{aligned}$$

We apply the lemma and rewrite the second term of (51) under the assumption of piecewise smooth functions on each subinterval $(\alpha_i, \alpha_{i+1}) \subset (0, 2\pi)^1$

¹We can divide the interval $[0, 2\pi]$ in the following way $[0, 2\pi] = [0 = \alpha_0, \alpha_1] \cup [\alpha_1, \alpha_2] \cup \dots \cup [\alpha_l, \alpha_{l+1} = 2\pi]$ so that z, m, n, s are piecewise smooth on each $[\alpha_i, \alpha_{i+1}]$.

$$\begin{aligned}
s(P)\Delta t \int_{\alpha_i}^{\alpha_{i+1}} \{szD_{\omega}^+[s] + D_{\omega}^-[m]s \sin \omega - D_{\omega}^-[n]s \cos \omega\} (Q(t^n, \omega))d\omega \\
= \int_{\alpha_i}^{\alpha_{i+1}} \{s(P)\Delta t szD_{\omega}^+[s] + ms \cos \omega + ns \sin \omega\} (Q(t^n, \omega)) d\omega \quad (52) \\
- \sin(\alpha_{i+1})m(Q(t^n, \alpha_{i+1})) + \sin(\alpha_i)m(Q(t^n, \alpha_i)) \\
+ \cos(\alpha_{i+1})n(Q(t^n, \alpha_{i+1})) - \cos(\alpha_i)n(Q(t^n, \alpha_i)) \\
\longrightarrow 0 \quad \text{as } \Delta t \rightarrow 0.
\end{aligned}$$

Analogously we obtain the limits of the double integrals in (46) and (47) for $\Delta t \rightarrow 0$

$$\begin{aligned}
s(P)\Delta t \int_{\alpha_i}^{\alpha_{i+1}} \cos \omega \{szD_{\omega}^+[s] + D_{\omega}^-[m]s \sin \omega - D_{\omega}^-[n]s \cos \omega\} (Q(t^n, \omega)) d\omega \\
= \int_{\alpha_i}^{\alpha_{i+1}} \{s(P)\Delta t \cos \omega szD_{\omega}^+[s] + ms(2 \cos^2 \omega - 1) + ns2 \sin \omega \cos \omega\} (Q(t^n, \omega)) d\omega \\
- \cos(\alpha_{i+1}) \sin(\alpha_{i+1})m(Q(t^n, \alpha_{i+1})) + \cos(\alpha_i) \sin(\alpha_i)m(Q(t^n, \alpha_i)) \\
+ \cos^2(\alpha_{i+1})n(Q(t^n, \alpha_{i+1})) - \cos^2(\alpha_i)n(Q(t^n, \alpha_i)) \\
\longrightarrow 0 \quad \text{as } \Delta t \rightarrow 0, \quad (53)
\end{aligned}$$

$$\begin{aligned}
s(P)\Delta t \int_{\alpha_i}^{\alpha_{i+1}} \sin \omega \{szD_{\omega}^+[s] + D_{\omega}^-[m]s \sin \omega - D_{\omega}^-[n]s \cos \omega\} (Q(t^n, \omega)) d\omega \\
= \int_{\alpha_i}^{\alpha_{i+1}} \{s(P)\Delta t \sin \omega szD_{\omega}^+[s] + ms2 \cos \omega \sin \omega + ns(1 - 2 \cos^2 \omega)\} (Q(t^n, \omega)) d\omega \\
- \sin^2(\alpha_{i+1})m(Q(t^n, \alpha_{i+1})) + \sin^2(\alpha_i)m(Q(t^n, \alpha_i)) \\
+ \cos(\alpha_{i+1}) \sin(\alpha_{i+1})n(Q(t^n, \alpha_{i+1})) - \cos(\alpha_i) \sin(\alpha_i)n(Q(t^n, \alpha_i)) \\
\longrightarrow 0 \quad \text{as } \Delta t \rightarrow 0. \quad (54)
\end{aligned}$$

Finally, we obtain the following approximation of (45)-(47) for $\Delta t \rightarrow 0$

$$\begin{aligned}
(sz)(P) &= \frac{1}{2\pi} \int_0^{2\pi} \{s(P)z^n - m^n \cos \omega - n^n \sin \omega\} (Q_{\tau}) d\omega \quad (55) \\
m(P) &= -\frac{1}{\pi} \int_0^{2\pi} \cos \omega \{s(P)z^n - m^n \cos \omega - n^n \sin \omega\} (Q_{\tau}) d\omega \\
n(P) &= -\frac{1}{\pi} \int_0^{2\pi} \sin \omega \{s(P)z^n - m^n \cos \omega - n^n \sin \omega\} (Q_{\tau}) d\omega,
\end{aligned}$$

where

$$Q_{\tau}(\omega) = \begin{pmatrix} x_p + \tau s \cos(\omega) \\ y_p + \tau s \sin(\omega) \end{pmatrix}.$$

Here, the local time step τ can be chosen arbitrary small, in particular we choose τ in such a way that the following condition holds

$$s \frac{\tau}{\Delta x} = CFL_g \leq 1 \quad (56)$$

with $s = s(P) = \frac{\sqrt{-b(P)}}{\varepsilon}$ and CFL_g being arbitrary small. The above evolution operator is denoted by EG_0^L .

3.2 Evolution operator for the nonlinear part

Let us recall the nonlinear part of the shallow water equations (2)

$$\begin{bmatrix} z \\ m \\ n \end{bmatrix}_t + \begin{bmatrix} 0 \\ \frac{m^2}{z-b} + \frac{1}{2\varepsilon^2} z^2 \\ \frac{mn}{z-b} \end{bmatrix}_x + \begin{bmatrix} 0 \\ \frac{mn}{z-b} \\ \frac{n^2}{z-b} + \frac{1}{2\varepsilon^2} z^2 \end{bmatrix}_y = 0. \quad (57)$$

Obviously z is constant in time. Analyzing the system (57) we find out that it creates a hyperbolic conservation law with the eigenvalues $\lambda_1 = 0$, $\lambda_2 = u \cos \theta + v \sin \theta$, $\lambda_3 = 2(u \cos \theta + v \sin \theta)$, $\theta \in [0, 2\pi)$. Let us consider the characteristic curve $\mathbf{x}(t) = (x(t), y(t))$ determined by the following equations

$$\frac{dx}{dt} = u, \quad \frac{dy}{dt} = v.$$

Time evolution of the momentum equation is determined by the following equations

$$\begin{aligned} \frac{Dm}{Dt} &= \left(u^2 - \frac{z}{\varepsilon^2}\right) z_x + uvz_y - u(m_x + n_y) - u(ub_x + vb_y) \\ \frac{Dn}{Dt} &= \left(v^2 - \frac{z}{\varepsilon^2}\right) z_y + uvz_x - v(m_x + n_y) - v(ub_x + vb_y), \end{aligned}$$

where

$$\frac{D}{Dt} := \frac{\partial}{\partial t} + u \frac{\partial}{\partial x} + v \frac{\partial}{\partial y}$$

denotes the time derivative along the characteristic $\mathbf{x}(t)$. Now, integrating along the characteristic $\mathbf{x}(t)$ we get

$$\begin{aligned} m^{n+1}(P) &= m^n(\mathbf{x}(t^n)) + \int_{t^n}^{t^{n+1}} \left[\left(u^2 - \frac{z}{\varepsilon^2}\right) z_x + uvz_y - u(m_x + n_y) - u(ub_x + vb_y) \right] (\mathbf{x}(t), t) dt \\ n^{n+1}(P) &= n^n(\mathbf{x}(t^n)) + \int_{t^n}^{t^{n+1}} \left[\left(v^2 - \frac{z}{\varepsilon^2}\right) z_y + uvz_x - v(m_x + n_y) - v(ub_x + vb_y) \right] (\mathbf{x}(t), t) dt. \end{aligned} \quad (58)$$

Denoting $\Delta t = t^{n+1} - t^n$ and approximating time integrals by means of the rectangle rule we obtain

$$\begin{aligned} m^{n+1}(P) &= \left[m + \Delta t \left\{ \left[u^2 - \frac{z}{\varepsilon^2} \right] z_x + uvz_y - u(m_x + n_y) - u(ub_x + vb_y) \right\} \right] (\mathbf{x}(t^n), t^n) \\ n^{n+1}(P) &= \left[n + \Delta t \left\{ \left[v^2 - \frac{z}{\varepsilon^2} \right] z_y + uvz_x - v(m_x + n_y) - v(ub_x + vb_y) \right\} \right] (\mathbf{x}(t^n), t^n). \end{aligned} \quad (59)$$

In order to evaluate (59) we had to freeze the characteristic direction and set

$$\frac{dx}{dt} = u(\mathbf{x}(t^n), t^n), \quad \frac{dy}{dt} = v(\mathbf{x}(t^n), t^n). \quad (60)$$

We denote the evolution operator (59) by $EG_{\Delta t}^{NL}$. Here the space derivatives in (59) can be approximated, e.g., by central differences.

4 Large time step finite volume schemes

In this section we will describe the large time step finite volume evolution Galerkin methods that combine the IMEX-type time discretizations and the approximate evolution operators for the linear part governing fast gravitational waves. The nonlinear advection part can be approximated either using the characteristic method, as described in Section 3.2, or by some standard numerical flux functions. Both approaches will be compared from the viewpoint of accuracy as well as asymptotic preserving property.

First, let us divide a computational domain Ω in a finite number of rectangular mesh cells C_{ij} , $(i, j) \in \mathbb{J}$, where \mathbb{J} is an index set. Denote by

$$f_{ij}^n := \frac{1}{|C_{ij}|} \int_{C_{ij}} f(x, t^n) dx$$

the cell average of a function f . For simplicity of presentation let us first consider the first order IMEX time discretization scheme (8). Second order time discretization schemes (9), (12) and (13) will be considered later analogously. Discretizing (8) in space by the finite volume method we obtain the following scheme

$$w_{ij}^{n+1} = w_{ij}^n - \frac{\Delta t}{|C_{ij}|} \int_{\partial C_{ij}} \mathcal{F}_L(w^{n+1}) \cdot \mathbf{n} ds - \frac{\Delta t}{|C_{ij}|} \int_{\partial C_{ij}} \mathcal{F}_{NL}(w^n) \cdot \mathbf{n} ds + \frac{\Delta t}{|C_{ij}|} \int_{C_{ij}} K(w^{n+1}) dx, \quad (61)$$

where $|C_{ij}|$ denotes the volume of the mesh cell C_{ij} , $|C_{ij}| = \Delta x \Delta y$, Δt is the time step and \mathbf{n} denotes the unit outer normal to ∂C_{ij} . In what follows we will describe how to approximate the cell interface integrals as well as the volume integral of the source term K . In particular, we will use the flux-vector splitting numerical flux of Van Leer [13] as well as the numerical fluxes based on the approximate evolution operators from Section 3.

Let us first approximate $\int_{\partial C_{ij}} \mathcal{F}_L(w^{n+1}) \cdot \mathbf{n} ds$. As already pointed out we predict the cell interface values for the linear operator by the approximate evolution operator EG_0^L . This is reasonable, since we take implicitly all infinitely many directions of the propagation of gravitational waves into account but omit the restrictive stability condition depending on $c_{ref} = \sqrt{gh_{ref}}$. More precisely, we set

$$\int_{\partial C_{ij}} \mathcal{F}_L(w^{n+1}) \cdot \mathbf{n} ds \approx \sum_j \gamma_j \mathcal{F}_L(EG_0^L(R(w^{n+1})(\mathbf{x}_j))) \cdot \mathbf{n}(\mathbf{x}_j) =: \mathcal{H}_{ij}^L(EG_0^L(Rw^{n+1})), \quad (62)$$

where γ_j, \mathbf{x}_j are weights and nodes of a suitable quadrature along the cell interfaces. In our numerical experiments we have used the Simpson rule. Further, the operator R is a

linear operator² that is either the identity or a reconstruction operator depending on the order of spatial approximation. In the numerical experiments we are using the following bilinear reconstruction for the second order schemes

$$\begin{aligned}
Rf|_{C_{ij}}(x_M + \tilde{x}, y_M + \tilde{y}) &= f_{ij} + \tilde{x}\delta_x^{ij}f + \tilde{y}\delta_y^{ij}f + \tilde{x}\tilde{y}\delta_{xy}^{ij}f \\
\delta_x^{ij}f &= \frac{2[f_{i+1,j} - f_{i-1,j}] + f_{i+1,j+1} + f_{i+1,j-1} - f_{i-1,j+1} - f_{i-1,j-1}}{8\Delta x} \\
\delta_y^{ij}f &= \frac{2[f_{i,j+1} - f_{i,j-1}] + f_{i+1,j+1} + f_{i-1,j+1} - f_{i+1,j-1} - f_{i-1,j-1}}{8\Delta y} \\
\delta_{xy}^{ij}f &= \frac{f_{i-1,j-1} + f_{i+1,j+1} - f_{i-1,j+1} - f_{i+1,j-1}}{4\Delta x\Delta y},
\end{aligned} \tag{63}$$

where (x_M, y_M) is the (bary)center of the cell C_{ij} and f stays for the equilibrium variables z, m, n .

Now in order to approximate the nonlinear flux term $\int_{\partial C_{ij}} \mathcal{F}_{NL}(w^n) \cdot \mathbf{n} ds$ we can either apply the approximate evolution operator derived in Section 3.2 or some standard one-dimensional numerical fluxes. In our numerical experiments presented in Section 5 the Van Leer numerical flux, c.f. [13], is used

$$\int_{\partial C_{ij}} \mathcal{F}_{NL}(w^n) \cdot \mathbf{n} ds \approx (F_{i+\frac{1}{2},j}^n - F_{i-\frac{1}{2},j}^n) \Delta x + (G_{i,j+\frac{1}{2}}^n - G_{i,j-\frac{1}{2}}^n) \Delta y =: \mathcal{H}_{ij}^{VL}(Rw^n), \tag{64}$$

here F and G are numerical fluxes in x, y -direction, respectively. More precisely, $F = \mathcal{F}_{NL} \cdot (1, 0)^T$ and $G = \mathcal{F}_{NL} \cdot (0, 1)^T$ and for the first order method we have

$$F_{i+\frac{1}{2},j}^n = \frac{1}{2} \left[F(w_{i+1,j}^n) + F(w_{ij}^n) - \left| \frac{dF}{dw} \left(\frac{w_{i+1,j}^n + w_{ij}^n}{2} \right) \right| (w_{i+1,j}^n - w_{ij}^n) \right]$$

with an analogous expressions for $F_{i-\frac{1}{2},j}$ as well as for $G_{i,j\pm\frac{1}{2}}$. The second order method is obtained via MUSCL-type approach using a bilinear reconstruction in space.

Another possibility is to use the approximate evolution operator (59) that in fact yields the characteristic method for the nonlinear part

$$\begin{aligned}
\int_{\partial C_{ij}} \mathcal{F}_{NL}(w^{n+\frac{1}{2}}) \cdot \mathbf{n} ds &\approx \sum_j \gamma_j \mathcal{F}_{NL}(EG_{\frac{\Delta t}{2}}^{NL}(Rw^n(\mathbf{x}_j))) \cdot \mathbf{n}(\mathbf{x}_j) \\
&=: \mathcal{H}_{ij}^{NL}(EG_{\frac{\Delta t}{2}}^{NL}(Rw^n)).
\end{aligned} \tag{65}$$

Here γ_j, \mathbf{x}_j are the weights and nodes of a numerical quadrature along the cell interfaces and R a reconstruction operator.

Finally the volume integral over K will be approximated in a well-balanced way. It means that suitable numerical quadratures in x - and y -directions are used, so that some

² Note that it is important that R is a linear operator to preserve the linearity of the approximation of gravitational waves.

important equilibrium states are preserved for discrete data exactly. In [32] the following well-balanced approximation of the source term has been used and shown to preserve the lake at rest states, i.e. $u = 0 = v, z = \text{const}$ equilibrium state exactly; see also [4, 5, 7, 10, 16, 24, 25, 26, 27] for other well-balanced schemes. In particular, if in (62) the Simpson rule is used, then the well-balanced approximation of the source term is as follows

$$\int_{C_{ij}} K(w^{n+1}) dx = \int_{C_{ij}} \left[\begin{array}{c} 0 \\ -\frac{z}{\varepsilon^2} \nabla b \end{array} \right] dx \approx -\frac{1}{\varepsilon^2} \sum_{k=-1}^1 \gamma_k \left[\begin{array}{c} 0 \\ \mu_x z_{i,j+\frac{k}{2}}^{*,n+1} \delta_x b_{i,j+\frac{k}{2}} \\ \mu_y z_{i+\frac{k}{2},j}^{*,n+1} \delta_y b_{i+\frac{k}{2},j} \end{array} \right] \quad (66)$$

$$=: \mathcal{K}_{ij}(EG_0^L(Rw^{n+1})),$$

where γ_k are the corresponding weights due to the Simpson rule, μ_x, δ_x are the averaging and central difference operators in x -direction. More precisely,

$$\mu_x z_{ij} = \frac{z_{i+\frac{1}{2},j} + z_{i-\frac{1}{2},j}}{2}, \quad \delta_x b_{ij} = \frac{b_{i+\frac{1}{2},j} - b_{i-\frac{1}{2},j}}{\Delta x},$$

analogous notation holds in the y -direction. Further, the values $z^{*,n+1}$ denote the predicted cell-interface values obtained as follows

$$w^{*,n+1} = EG_0^L(R(w^{n+1})).$$

4.1 First order schemes

In summary, the first order finite volume scheme with the IMEX-type time discretization (8) is given in the following way

$$w_{ij}^{n+1} = w_{ij}^n - \frac{\Delta t}{|C_{ij}|} \left(\mathcal{H}_{ij}^L(EG_0^L(w^{n+1})) + \mathcal{H}_{ij}^{VL}(w^n) - \mathcal{K}_{ij}(EG_0^L(w^{n+1})) \right) \quad (67)$$

or

$$w_{ij}^{n+1} = w_{ij}^n - \frac{\Delta t}{|C_{ij}|} \left(\mathcal{H}_{ij}^L(EG_0^L(w^{n+1})) + \mathcal{H}_{ij}^{NL}(EG_{\frac{\Delta t}{2}}^{NL}(w^n)) - \mathcal{K}_{ij}(EG_0^L(w^{n+1})) \right). \quad (68)$$

4.2 Second order schemes

In order to derive the second order schemes we apply in space the bilinear reconstruction (63) and either RK2CN scheme (9) or the BDF-type time discretizations (12) and (13). These time discretizations belong to the class of IMEX-type schemes.

Applying the RK2CN time discretization (9), the van Leer numerical flux for the nonlinear operator and the local approximate evolution operator EG_0^L for the linear part we obtain the following fully discrete scheme

$$\begin{aligned} w_{ij}^{n+\frac{1}{2}} &= w_{ij}^n - \frac{\Delta t}{2|C_{ij}|} \left(\mathcal{H}_{ij}^L(EG_0^L(Rw^{n+1/2})) + \mathcal{H}_{ij}^{VL}(Rw^n) - \mathcal{K}_{ij}(EG_0^L(Rw^{n+1/2})) \right), \\ w_{ij}^{n+1} &= w_{ij}^n - \frac{\Delta t}{2|C_{ij}|} \left(\mathcal{H}_{ij}^L(EG_0^L(Rw^{n+1})) + \mathcal{H}_{ij}^L(EG_0^L(Rw^n)) + 2\mathcal{H}_{ij}^{VL}(Rw^{n+1/2}) \right) \\ &\quad + \frac{\Delta t}{2|C_{ij}|} \left(\mathcal{K}_{ij}(EG_0^L(Rw^n)) + \mathcal{K}_{ij}(EG_0^L(Rw^{n+1})) \right). \end{aligned} \quad (69)$$

Similarly, using the BDF time discretization (12) instead, the local evolution operator EG_0^L for the linear and the van Leer numerical flux for the nonlinear part, we obtain

$$\begin{aligned} w_{ij}^{n+1} &= \alpha_0 w_{ij}^n + \alpha_1 w_{ij}^{n-1} \\ &\quad - \frac{1}{|C_{ij}|} \beta \mathcal{H}_{ij}^L(EG_0^L(Rw^{n+1})) + \beta_0 \mathcal{H}_{ij}^{VL}(Rw^n) + \beta_1 \mathcal{H}_{ij}^{VL}(Rw^{n-1}) \\ &\quad + \frac{\beta}{|C_{ij}|} \mathcal{K}_{ij}(EG_0^L(Rw^{n+1})). \end{aligned} \quad (70)$$

Using (13) and predict a solution at half time steps by means of the approximate evolution operator $EG_{\frac{\Delta t}{2}}^{NL}$ for the nonlinear advection part we obtain

$$\begin{aligned} w_{ij}^{n+1} &= \alpha_0 w_{ij}^n + \alpha_1 w_{ij}^{n-1} \\ &\quad - \frac{1}{|C_{ij}|} \beta \mathcal{H}_{ij}^L(EG_0^L(Rw^{n+1})) + \tilde{\beta}_0 \mathcal{H}_{ij}^{NL}(EG_{\frac{\Delta t}{2}}^{NL}(Rw^n)) + \tilde{\beta}_1 \mathcal{H}_{ij}^{NL}(EG_{\frac{\Delta t}{2}}^{NL}(Rw^{n-1})) \\ &\quad + \frac{\beta}{|C_{ij}|} \mathcal{K}_{ij}(EG_0^L(Rw^{n+1})), \end{aligned} \quad (71)$$

where $\tilde{\beta}_k$, $k = 0, 1$, are the corresponding interpolation coefficients.

4.3 Well-balanced property

The aim of this subsection is to show that our IMEX large time step schemes are well-balanced for the lake at rest. Let us first consider the first order semi-discrete scheme, cf. (8),

$$w^{n+1} + \Delta t (\nabla \cdot \mathcal{F}_L - K)(w^{n+1}) = w^n - \Delta t \nabla \cdot \mathcal{F}_{NL}(w^n). \quad (72)$$

Further, let us assume that at time step t^n the discrete solution w^n is the lake at rest solution, i.e. $z = \text{const.}$, $m = n = 0$. Then the nonlinear flux $\mathcal{F}_{NL}(w^n) = 0$. Denoting $\Phi(w) := (\nabla \cdot \mathcal{F}_L - K)(w)$, we obtain from (72) that

$$w^{n+1} + \Delta t \Phi(w^{n+1}) = \begin{bmatrix} z^{n+1} \\ \mathbf{m}^{n+1} \end{bmatrix} + \Delta t \begin{bmatrix} \nabla \cdot \mathbf{m}^{n+1} \\ -\frac{b}{\varepsilon^2} \nabla z^{n+1} \end{bmatrix} = w^n. \quad (73)$$

Consequently, the lake at rest is one solution of (73) and $w^{n+1} = w^n$.

Lemma 4.1 *Let $\Omega \subset \mathbb{R}^2$ be a bounded Lipschitz-continuous domain and the bottom topography $b \in W^{1,\infty}(\Omega)$, $b \leq 0$. Then the following problem*

$$w + \Delta t \Phi(w) = 0 \quad (74)$$

has a unique solution $w \in H^1(\Omega)$, provided

$$\int_{\partial\Omega} bz \partial_\nu z \, ds \geq 0. \quad (75)$$

Proof: From the equation (74) it follows that $z = -\Delta t \nabla \cdot \mathbf{m}$ and $\mathbf{m} = \Delta t \frac{b}{\varepsilon^2} \nabla z$. Plugging the momentum \mathbf{m} into the equation for the perturbation z , we obtain the following elliptic eigenvalue problem

$$-\nabla \cdot (b \nabla z) = \lambda z, \quad \lambda := \frac{\varepsilon^2}{\Delta t^2} > 0. \quad (76)$$

Let us multiply (76) with z and integrate over the domain Ω

$$0 \leq \lambda \|z\|_{L^2(\Omega)}^2 = \langle z, -\nabla(b \nabla z) \rangle_{L^2(\Omega)} = \int_{\Omega} b \nabla z \cdot \nabla z \, d\mathbf{x} - \int_{\partial\Omega} b z \partial_\nu z \, ds \leq 0. \quad (77)$$

Therefore $z = 0$ and hence $\mathbf{m} = 0$. Consequently, there exists the only one solution of the problem (73), which is the lake at rest solution $z = 0$ and $u = 0 = v$. \square

Let us note that the above condition on the boundary integral (75) is satisfied in many practical situations; for example, when the homogeneous Dirichlet or Neumann boundary conditions are assumed for the perturbation z or in the case of periodic boundary conditions.

Corollary 4.2 *The first order schemes (67), (68) are well-balanced for the lake at rest uniformly with respect to the Froude number $\varepsilon > 0$.*

Proof: Lemma 4.1 implies that by starting initially from the lake at rest solution, we get by the first order semi-discrete scheme a new solution $w^{n+1} = (\text{const.}, 0, 0)$, that is again a lake at rest solution.

Indeed, as we have shown by Lemma 4.1 the time discretization yields $w^{n+1} = w^n$. It is easy to show that the space discretization of the linear flux $\mathcal{F}_L(w^{n+1})$ and of the source term $K(w^{n+1})$ preserves the well-balance property in space, too. More precisely, the space discretization of $\mathcal{F}_L(w^{n+1})$ yields for the momentum equation in the x -direction the following approximation, cf. (62)

$$\int_{\partial C_{ij}} -\frac{1}{\varepsilon^2} b(x, y) z^{n+1}(x, y) n_x \, ds \approx -\frac{1}{\varepsilon^2} \sum_{k=-1}^1 \gamma_k \delta_x (z^{*,n+1} b)_{i, j + \frac{k}{2}}. \quad (78)$$

On the other hand the space discretization of the source term yields according to (66) for the momentum in the x -direction

$$\int_{C_{ij}} K(w^{n+1}) \, dx \approx -\frac{1}{\varepsilon^2} \sum_{k=-1}^1 \gamma_k \mu_x z_{i, j + \frac{k}{2}}^{*,n+1} \delta_x b_{i, j + \frac{k}{2}}. \quad (79)$$

Analogous relations hold for the y -direction. From (78) and (79) it is easy to see that the space discretization of the linear fluxes balances out the source term discretization, provided $z^{*,n+1} = \text{const.}$ But this is a consequence of Lemma 4.1 and of the fact that the evolution operator (55) is well-balanced for the lake at rest. The latter can be verified directly by plugging the lake at rest solution in the evolution operator; see also [32]. \square

Realizing that $w = (z, m, n)$ are in fact the equilibrium variables for the lake at rest state, we obtain that the bilinear reconstruction Rw , cf. (63), preserves the lake at rest conditions $(z, m, n) = (\text{const.}, 0, 0)$. Now applying the analogous arguments as for the first order schemes the following result follows, too.

Corollary 4.3 *The second order schemes (69),(70),(71) are well-balanced for the lake at rest uniformly with respect to the Froude number $\varepsilon > 0$.*

4.4 Summary of the algorithm

In what follows we give a brief summary of the algorithms for our large time step schemes. We present the algorithms for the first order schemes (67), (68) and for the second order schemes (70), (71). Algorithm for the RK2CN scheme (69) is analogous.

Let us denote by \mathbf{w} the column vector containing all cell averages, $\mathbf{w} = (w_{ij})_{(i,j) \in J}^T$, where J is the set of all cell indices (i, j) . Recall that $w_{ij} = (z_{ij}, m_{ij}, n_{ij})^T$. Then, we can rewrite the first order large time step schemes symbolically in the following way

$$(\mathbf{Id} + \Delta t \mathbf{A}) \mathbf{w}^{n+1} = RHS(\mathbf{w}^n), \quad (80)$$

where the matrix \mathbf{A} contains (constant) coefficients arising from the interface integrals of the linear flux and of the source term composed with the linear evolution operator, i.e. $\frac{1}{|C_{ij}|} \left(\mathcal{H}_{ij}^L(EG_0^L(w^{n+1})) - \mathcal{K}_{ij}(EG_0^L(w^{n+1})) \right)$. The right hand side vector $RHS(\mathbf{w}^n)$ is composed from a sum of \mathbf{w}^n and the terms arising from the discretization of the nonlinear flux interface integrals $\frac{-\Delta t}{|C_{ij}|} \mathcal{H}_{ij}^{VL}(w^n)$ or $\frac{-\Delta t}{|C_{ij}|} \mathcal{H}_{ij}^{NL}(EG_{\frac{\Delta t}{2}}^{NL}(w^n))$ by applying the scheme (67) or (68), respectively.

Algorithm 1 First order schemes (67) or (68)

Input: Vector \mathbf{w} contains the initial conditions for cell averages of z, m, n for all finite volume cells

- 1: assemble the matrix \mathbf{A} , cf. (80), according to (67) or (68) and (55)
 - 2: $t = 0$
 - 3: **while** $t < T_{final}$ **do**
 - 4: compute Δt according to (7)
 - 5: compute the right hand side of (80); $RHS := RHS(\mathbf{w})$
 - 6: solve $(\mathbf{Id} + \Delta t \mathbf{A}) \mathbf{w} = RHS$
 - 7: update time; $t := t + \Delta t$
 - 8: **end while**
-

Analogously, we can rewrite the large time step second order BDF-type schemes (70) or (71) in the following way

$$(\mathbf{Id} - \beta \mathbf{A}) \mathbf{w}^{n+1} = RHS(\mathbf{w}^n, \mathbf{w}^{n-1}), \quad (81)$$

where $\beta < 0$ is given in Table 1, $RHS(\mathbf{w}^n, \mathbf{w}^{n-1})$ is the right hand side vector arising from the sum of $\alpha_0 \mathbf{w}^n + \alpha_1 \mathbf{w}^{n-1}$ and from the discretization of the nonlinear flux interface integrals $\frac{-\tilde{\beta}_0}{|C_{ij}|} \mathcal{H}_{ij}^{NL}(EG_{\frac{\Delta t}{2}}^{NL}(Rw^n)) - \frac{\tilde{\beta}_1}{|C_{ij}|} \mathcal{H}_{ij}^{NL}(EG_{\frac{\Delta t}{2}}^{NL}(Rw^{n-1}))$ with the coefficients $\alpha_i, \tilde{\beta}_i, \beta$, $i = 1, 2$, given in Section 2. Analogous expression of the RHS holds for the second order BDF-type scheme (70) with the Van Leer numerical flux for the nonlinear flux terms.

Algorithm 2 BDF-type second order schemes (70) or (71)

Input: Vector \mathbf{w}_{old} contains the initial conditions for cell averages of z, m, n for all finite volume cells and the vector \mathbf{w} the solution after the first time step obtained, e.g., by (69)

- 1: assemble the matrix \mathbf{A} , cf. (81), according to (70) or (71) and (55)
 - 2: $t = 0$
 - 3: **while** $t < T_{final}$ **do**
 - 4: compute Δt according to (7)
 - 5: reconstruct \mathbf{w} using (63)
 - 6: compute the right hand side of (81); $RHS := RHS(\mathbf{w}, \mathbf{w}_{old})$
 - 7: $\mathbf{w}_{old} := \mathbf{w}$
 - 8: solve $(\mathbf{Id} - \beta \mathbf{A})\mathbf{w} = RHS$
 - 9: update time; $t := t + \Delta t$
 - 10: **end while**
-

5 Numerical experiments

In the previous sections we have proposed new first and second order large time step schemes for the shallow water equations (2). Our aim now is to analyze their behaviour on a series of numerical experiments and compare their accuracy, stability and asymptotic behaviour with respect to small Froude number. In order to easily refer to different variants of our large time step schemes we introduce here the following abbreviations: the first order IMEX-type scheme (67) will be denoted by VLO1, if the van Leer numerical flux for the nonlinear flux is used and by CHARO1, respectively, if the characteristic scheme is used for the nonlinear flux, cf. (68). Further, the second order IMEX-type scheme based on the Runge-Kutta Cranck Nicolson approximation (69) is denoted by RK2CN and the two variants of the BDF scheme (70) and (71) by BDFVLO2 and BDFCHARO2, respectively.

5.1 Traveling vortex

In [40] an analytical solution to the two-dimensional shallow water equations for the so-called traveling vortex experiments has been presented, see also [44] for further experiments. The computational domain is a unit square $[0, 1] \times [0, 1]$. We use the periodic boundary conditions in x -direction, the absorbing boundary conditions in y -direction and

the following initial conditions

$$\begin{aligned}
h(x, y, 0) &= 110 + \begin{cases} \left(\frac{\varepsilon\Gamma}{\omega}\right)^2 (k(\omega r_c) - k(\pi)) & \text{if } \omega r_c \leq \pi \\ 0 & \text{otherwise} \end{cases} \\
u(x, y, 0) &= 0.6 + \begin{cases} \Gamma(1 + \cos(\omega r_c))(0.5 - y) & \text{if } \omega r_c \leq \pi \\ 0 & \text{otherwise} \end{cases} \\
v(x, y, 0) &= \begin{cases} \Gamma(1 + \cos(\omega r_c))(x - 0.5) & \text{if } \omega r_c \leq \pi \\ 0 & \text{otherwise} \end{cases} \\
r_c &= \|\mathbf{x} - (0.5, 0.5)\|, \quad \Gamma = 1.5, \quad \omega = 4\pi \\
k(r) &= 2 \cos(r) + 2r \sin(r) + \frac{1}{8} \cos(2r) + \frac{r}{4} \sin(2r) + \frac{3}{4} r^2.
\end{aligned} \tag{82}$$

A rotating vortex initially positioned at $(0.5, 0.5)$ is transported by the uniform flow with the advection velocity $\mathbf{u}_{\text{ref}} = (0.6, 0)$ to the right. Due to the periodic boundary conditions the exact solution is periodic with the period $T = 5/3$.

$$\begin{aligned}
h(x, y, t) &= h(x - t/T, y, 0) \\
u(x, y, t) &= u(x - t/T, y, 0) \\
v(x, y, t) &= v(x - t/T, y, 0).
\end{aligned} \tag{83}$$

In Figure 2, 3, 4 numerical solutions for $\varepsilon = 0.8, 0.01$ and 0.05 using 160×160 mesh cells are shown, respectively. Time evolution is controlled by the CFL condition (7), where CFL_u is set to 0.45 in the experiments presented in Figures 2,4 and to 0.9 in Figure 3. For the local evolution operator EG_0^L we set CFL_g to 0.01. Note that this parameter just controls small local time step τ in the predictor step EG_0^L but has no influence on the actual time step Δt of the large time step finite volume update.

In Figures 2,3 results obtained by the second order BDFVLO2 scheme (70) are presented for $\varepsilon = 0.8$ and $\varepsilon = 0.01$, respectively. In both figures we can also see time evolution of the CFL numbers, cf. (3), up to time $T = 0.1$. For small ε , $\varepsilon = 0.01$, the CFL numbers may raise dramatically, reaching even the values up to 69. In Figure 4 we have compared for the Froude number $\varepsilon = 0.05$ horizontal cuts at $x = 0.5$ and $x = 0.56$ of all presented large time step finite volume schemes with the analytical solution at times $T = 0.1$ and $5/3$, respectively, using a mesh 160×160 cells. We can clearly see that the first order schemes are quite diffusive; after one time period at $T = 5/3$ the local maximum of the approximate solutions is reduced strongly. On the other hand the second order schemes still approximate local extrema quite accurately. We can notice that the second order RK2CN and the BDFVLO2 scheme yield almost identical results. On the other hand the BDFCHARO2 scheme yields more diffusive results. This can be explained in the following way: in the characteristic based BDF-type scheme (71) the nonlinear evolution operator $EG_{\Delta t}^{NL}$ corresponds only to a nonlinear subsystem; it does not give any information about the intermediate solution of the whole hyperbolic conservation at $t^{n+1/2}$. Consequently, we only have by the Taylor expansion that $\|w^{n+1/2} - EG_{\frac{\Delta t}{2}}^{NL}(w^n)\| = \mathcal{O}(\Delta t)$ and the local truncation error for (71) is only of second order. For other second order IMEX-type schemes the local truncation error is of third order. Numerical experiments for the experimental order of convergence, presented below, also indicate that the smaller the

Froude number ε is, the higher the accuracy of the BDFCHARO2, cf. Table 6. Thus, the effects due to a larger local truncation error in the characteristic scheme is less dominant.

Still the results obtained by our large time step schemes are less dissipative than those obtained by fully explicit schemes, due to much larger time steps that are allowed by (7). See Figure 5, where we have compared for $\varepsilon = 0.001$ the L^1 - errors of the explicit second order FVEG scheme derived in [32] and our new IMEX-type schemes; in particular we plot here results for the BDFVLO2 scheme, but the others behave analogously. Moreover we also present time evolution of the relative kinetic energy $\frac{1}{2}h(t)|\mathbf{u}(t)|^2/\frac{1}{2}h(0)|\mathbf{u}(0)|^2$ for two different mesh resolution with 80×80 and 160×160 cells. We can see clearly that the energy decay is more profound in the case of explicit FVEG scheme than for semi-implicit BDFVLO2 scheme.

Tables 2-6 present results of the experimental order of convergence (EOC) for the first and second order large time step finite volume schemes VLO1 (67), CHARO1 (68), RK2CN (69), BDFVLO2 (70) and BDFCHARO2 (71). Here the EOC is computed using the following formula

$$EOC = \log_2 \left(\frac{\|w_N - w\|}{\|w_{2N} - w\|} \right),$$

where w_N is the approximate solution on a mesh with $N \times N$ mesh cells and w is the exact reference solution. Results computed for various Froude numbers $\varepsilon = 0.8, 0.05$ and 0.01 demonstrate asymptotic preserving property for both the first as well as second order schemes. Indeed, depending on the order of time/space discretization we obtain the first or second order EOC uniformly with respect to ε . Moreover, we can notice that for smaller ε the EOC increases, e.g. for $\varepsilon = 0.01$ the EOC of the second order schemes is around $2.3 \sim 2.4$. Concerning the efficiency of the approximative schemes we would like to point out that CFL_u -number for the RK2CN scheme (69) is half of the corresponding CFL_u -number for the BDFVLO2 scheme (70). Consequently, computational costs for both schemes are comparable, since the number of linear systems to be solved is the same.

If in addition bottom topography is non-constant more complex wave pattern develops. In Figures 6, 7 we have plotted time evolution of the water depth h and its isolines for bottom topography $\tilde{b} = 10 \exp(-5(x-1)^2 - 50(y-0.5)^2)$ and Froude number $\varepsilon = 0.05$. We can clearly identify a periodic sine-type gravitational wave as well as advected vortex structure. Time instants are $T = 0, 0.24, 0.71, 1.18, 1.65$ and 2.35 . Time step is controlled only by advection, i.e. $CFL_u = 0.45$. This leads to CFL numbers from 7.1 to 7.5. The solution presented in Figures 6, 7 is computed by the second order BDFVLO2 scheme. The results obtained by other second order methods, not presented here, are analogous.

5.2 Sine wave evolution

In this experiment we study behaviour of our large time step schemes on smooth solutions for small Froude numbers. In [12] Degond and Tang provided an asymptotic preserving all Mach number scheme for the isentropic Euler equations. Comparing the mathematical structure of the isentropic Euler equations and the homogeneous shallow water equations (1) we can notice that both are analogous when identifying the water depth h with the

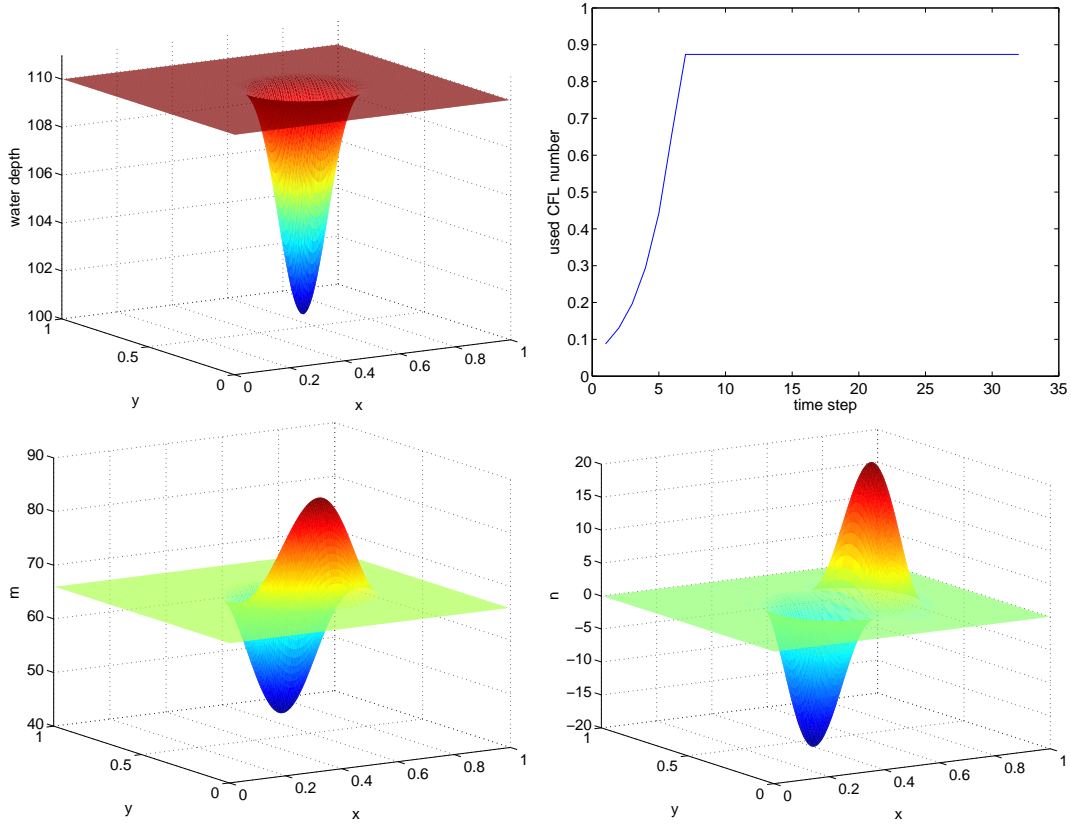


Figure 2: Numerical solution of the traveling vortex experiment at time $T = 0.1$ computed with the second order BDFVLO2 scheme, the Froude number $\varepsilon = 0.8$ and $CFL_u = 0.45$. The pictures show (from top to bottom and left to right): water depth, CFL numbers used and the first and second momentum component m, n .

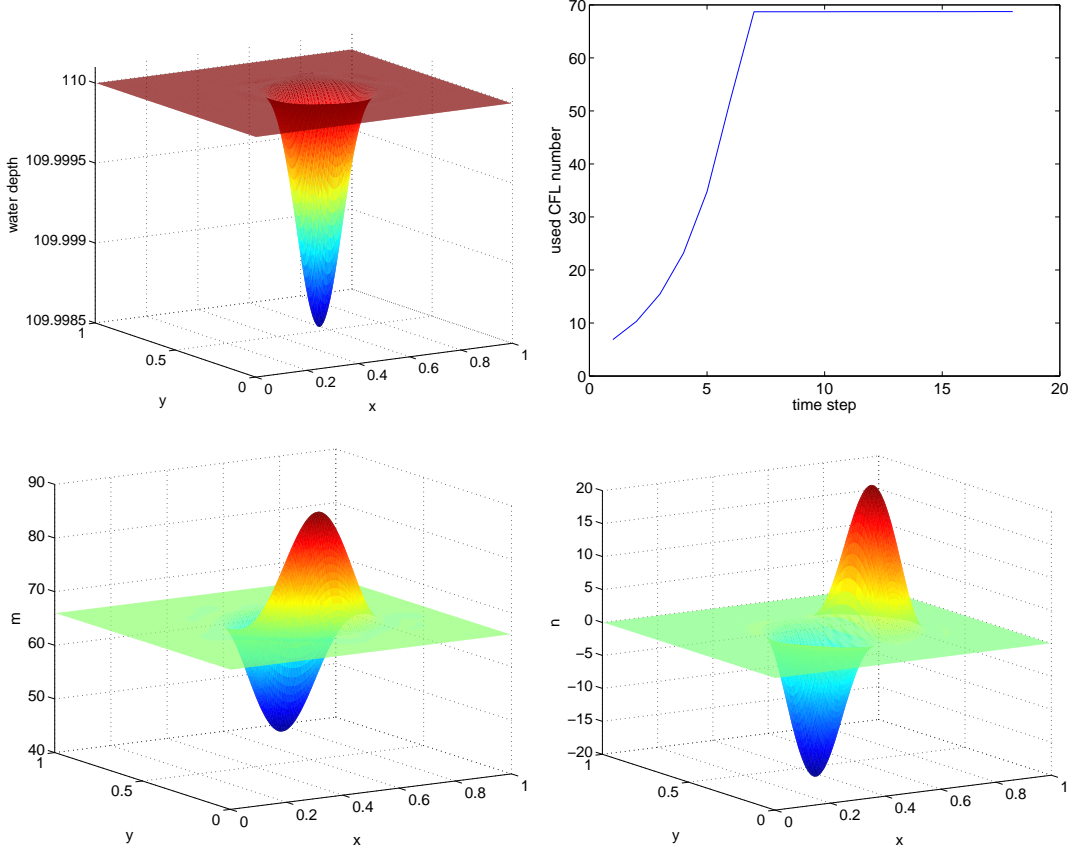


Figure 3: Numerical solution of the traveling vortex experiment at time $T = 0.1$ computed with the second order BDFVLO2 scheme, the Froude number $\varepsilon = 0.01$ and $CFL_u = 0.9$. The pictures show (from top to bottom and left to right): water depth, CFL numbers used and the first and second momentum component m, n .

gas density ρ and setting the equation of state for compressible gas to be $p(\rho) := \frac{1}{2}\rho^2$. This allows us to compare our results with the results presented in [12].

We consider a computational domain $[0, 1] \times [0, 1]$, use periodic boundary conditions and the following initial conditions

$$\begin{aligned}
 h(x, y, 0) &= 1 + \varepsilon^2 \sin^2(2\pi(x + y)) \\
 m(x, y, 0) &= \sin(2\pi(x - y)) + \varepsilon^2 \sin(2\pi(x + y)) \\
 n(x, y, 0) &= \sin(2\pi(x - y)) + \varepsilon^2 \cos(2\pi(x + y)).
 \end{aligned} \tag{84}$$

In Figure 8, 9 numerical solutions for $\varepsilon = 0.05$ and 0.01 , respectively, on a mesh with 160×160 cells at $T = 1$ are shown. Results are obtained by the BDFCHARO2 scheme (71) using the nonlinear operator EG^{NL} (59). We set $CFL_u = 0.6$ that yields the total CFL around 18 for $\varepsilon = 0.05$ and around 85 for $\varepsilon = 0.01$. For the local linear operator EG_0^L the local time step τ is obtained using the corresponding $CFL_g = 0.01$.

We can clearly see that z and $\partial_x m + \partial_y n$ converge to 0 as far as ε goes to 0. Indeed, $z = \mathcal{O}(10^{-6})$, $\partial_x m + \partial_y n = \mathcal{O}(10^{-4})$ for $\varepsilon = 0.05$ and $z = \mathcal{O}(10^{-9})$, $\partial_x m + \partial_y n = \mathcal{O}(10^{-6})$ for $\varepsilon = 0.01$. Our results for $\varepsilon = 0.05$ are analogous to those of Degond and Tang [12].

$$\varepsilon = 0.8, CFL_u = 0.45, CFL \approx 0.9, T = 0.1$$

N	L^1 -error in z	EOC	L^1 -error in m	EOC	L^1 -error in n	EOC
20	0.21019		0.50860		0.44681	
40	0.14303	0.55539	0.29634	0.77926	0.25680	0.79900
80	0.08408	0.76648	0.16136	0.87697	0.13759	0.90028
160	0.04578	0.87704	0.08455	0.93239	0.07160	0.94225

$$\varepsilon = 0.05, CFL_u = 0.45, CFL \approx 7.25, T = 0.1$$

N	L^1 -error in z	EOC	L^1 -error in m	EOC	L^1 -error in n	EOC
20	0.00408		1.18800		1.16980	
40	0.00320	0.34894	0.87983	0.43328	0.87707	0.41547
80	0.00210	0.60779	0.57048	0.62504	0.57483	0.60955
160	0.00123	0.77580	0.33396	0.77250	0.33783	0.76682

Table 2: Experimental order of convergence for the first order VLO1 scheme; traveling vortex test.

5.3 Lake at rest steady state

The aim of this experiment is to demonstrate experimentally that our newly developed large time step schemes are indeed well-balanced for the lake at rest state. To this end let us consider the following experiment proposed by Canestrelli et al. in [10]. We consider the shallow water system (2) with a smooth

$$\tilde{b}_s(x, y) = 5 \exp\left(-\frac{2}{5}((x-5)^2 + (y-5)^2)\right) \quad (85)$$

and a discontinuous

$$\tilde{b}_d(x, y) = \begin{cases} 4 & \text{if } 4 \leq x, y \leq 8 \\ 0 & \text{else} \end{cases} \quad (86)$$

bottom topography. The initial condition is a lake at rest state with $h + \tilde{b} = 10$ and $m = n = 0$. We have computed numerical solutions for all schemes and different RBC constants. The L^1 - and L^∞ -errors of the water depth z , $z = h + b$, $b = \tilde{b} - RBC$, and the specific discharge $q = \sqrt{m^2 + n^2}$ at $T = 10$ are presented in Table 7. Numerical solution is computed using a mesh with 45×45 cells. We can notice that using a particular value for the RBC constant, i.e. $h + \tilde{b} = RBC = 10$, we have a special lake at rest state $z = m = n = 0$. In this case, the right-hand side of the linear system obtained after the finite volume update is zero. Consequently, the numerical solution for the next time step is zero and the error between a numerical and exact solution is zero, as well.

Furthermore, our results presented in Table 7 demonstrate clearly, that all large time step schemes derived in the paper preserve the lake at rest steady state also for other values of RBC , the difference between the numerical and exact solution is only due to round-off errors.

$$\varepsilon = 0.8, CFL_u = 0.45, CFL \approx 0.9, T = 0.1$$

N	L^1 -error in z	EOC	L^1 -error in m	EOC	L^1 -error in n	EOC
20	0.19721		0.45503		0.42936	
40	0.13170	0.58251	0.26401	0.78537	0.24486	0.81021
80	0.07813	0.75324	0.14160	0.89881	0.13177	0.89399
160	0.04323	0.85400	0.07374	0.94123	0.06960	0.92092

$$\varepsilon = 0.05, CFL_u = 0.45, CFL \approx 7.25, T = 0.1$$

N	L^1 -error in z	EOC	L^1 -error in m	EOC	L^1 -error in n	EOC
20	0.00400		1.17950		1.15880	
40	0.00314	0.34839	0.87069	0.43792	0.86655	0.41925
80	0.00206	0.60798	0.56184	0.63200	0.56670	0.61269
160	0.00120	0.77839	0.32800	0.77644	0.33262	0.76871

Table 3: Experimental order of convergence for the first order CHARO1 scheme; traveling vortex test.

6 Conclusion

In the present paper we have derived and analyzed new large time step finite volume schemes for the shallow water flows with low Froude numbers. The main idea of the method is to split the nonlinear shallow water equations into the linear part describing the gravitational waves and the nonlinear part modelling the nonlinear advection. We have used IMEX-type time discretization to approximate linear waves implicitly and nonlinear explicitly. Consequently, time step is dictated only by the flow velocity \mathbf{u} , cf. (7). In present paper we have tested for time discretization first order implicit-explicit Euler scheme (8), second order Runge Kutta Cranck Nicolson (9) and second order BDF scheme (11).

The novelty of our approach lies in approximating fast gravitational waves in a truly multidimensional way. To this end the approximate evolution operator EG_0^L is derived using the theory of bicharacteristics. Further, the nonlinear advection is approximated either by means of the characteristic method EG^{NL} or by using some standard nonlinear flux function. In our experiments we have chosen the van Leer flux that belongs to the class of flux-vector splitting schemes, but any standard numerical flux for the hyperbolic conservation laws may be used as well. The above combinations yield two first order (67), (68) and three second order (69), (70), (71) large time step finite volume schemes. In Section 2 we have proven theoretically that the proposed time approximations yield asymptotic preserving schemes. In future we want to analyse theoretically the asymptotic preserving property also for spatial discretization. Fully discrete large time step finite volume schemes for both first and second order are derived in Section 4, where the well-balanced property is studied as well. Analyzing the underlying elliptic eigenvalue problem (76) that follows from our splitting approach, we are able to prove that both the first as well as second order time discretizations yield well-balanced semi-discrete schemes. In order to approximate the source term integrals we apply a suitable quadrature rule (79),

$$\varepsilon = 0.8, CFL_u = 0.9, CFL \approx 1.75, T = 0.1$$

N	L^1 -error in z	EOC	L^1 -error in m	EOC	L^1 -error in n	EOC
20	0.06944		0.17415		0.18840	
40	0.01584	2.1323	0.03977	2.1306	0.05377	1.8089
80	0.00327	2.2766	0.00906	2.1349	0.01609	1.7407
160	0.00085	1.9419	0.00230	1.9780	0.00445	1.8534

$$\varepsilon = 0.05, CFL_u = 0.9, CFL \approx 14.5, T = 0.1$$

N	L^1 -error in z	EOC	L^1 -error in m	EOC	L^1 -error in n	EOC
20	0.00240		0.49009		0.50795	
40	0.00067	1.8431	0.11370	2.1078	0.12483	2.0248
80	0.00019	1.8415	0.02305	2.3023	0.02788	2.1627
160	3.89e-5	2.2637	0.00469	2.2984	0.00650	2.0996

$$\varepsilon = 0.01, CFL_u = 0.9, CFL \approx 69, T = 0.1$$

N	L^1 -error in z	EOC	L^1 -error in m	EOC	L^1 -error in n	EOC
20	5.07e-4		1.14180		1.17160	
40	1.23e-4	2.0472	0.35999	1.6653	0.36423	1.6855
80	3.20e-5	1.9363	0.07283	2.3054	0.07454	2.2888
160	8.25e-6	1.9569	0.01347	2.4348	0.01434	2.3781

Table 4: Experimental order of convergence for the second order RK2CN scheme; traveling vortex test.

that yields a preservation of the lake at rest steady state in space as well. We want to point out that the well-balanced property holds uniformly with respect to ε .

Numerical experiments presented in Section 5 demonstrate clearly that the proposed large time step finite volume schemes yield accurate, stable, well-balanced and asymptotic preserving approximation for low Froude number flows.

7 Appendix

7.1 Derivation of the Exact Integral Representation

In what follows our aim is to present the derivation of the exact integral representation (45)-(47). Due to the symmetry of (43) for any fixed values (P, ω) we have

$$\begin{aligned}
 \mathbf{x}^1(t, \omega) &= \mathbf{x}^3(t, \omega + \pi) & \mathbf{x}^3(t, \omega) &= \mathbf{x}^1(t, \omega + \pi) \\
 \mathbf{y}^1(t, \omega) &= \mathbf{y}^3(t, \omega + \pi) & \mathbf{y}^3(t, \omega) &= \mathbf{y}^1(t, \omega + \pi) \\
 \theta^1(t, \omega) + \pi &= \theta^3(t, \omega + \pi) & \theta^3(t, \omega) + \pi &= \theta^1(t, \omega + \pi) \\
 \theta_t^1(t, \omega) &= \theta_t^3(t, \omega + \pi) & \theta_t^3(t, \omega) &= \theta_t^1(t, \omega + \pi)
 \end{aligned} \tag{87}$$

$$\varepsilon = 0.8, CFL_u = 0.45, CFL \approx 0.9, T = 0.1$$

N	L^1 -error in z	EOC	L^1 -error in m	EOC	L^1 -error in n	EOC
20	0.071621		0.17748		0.19415	
40	0.017248	2.0539	0.03939	2.1717	0.05861	1.7279
80	0.003682	2.2277	0.00898	2.1339	0.01670	1.8115
160	0.000979	1.9119	0.00227	1.9838	0.00456	1.8721

$$\varepsilon = 0.05, CFL_u = 0.45, CFL \approx 7.25, T = 0.1$$

N	L^1 -error in z	EOC	L^1 -error in m	EOC	L^1 -error in n	EOC
20	0.00151		0.49335		0.51883	
40	3.07e-4	2.2999	0.11430	2.1098	0.12815	2.0175
80	5.36e-5	2.5146	0.02224	2.3616	0.02782	2.2036
160	1.51e-5	1.8287	0.00458	2.2813	0.00650	2.0971

$$\varepsilon = 0.01, CFL_u = 0.45, CFL \approx 35, T = 0.1$$

N	L^1 -error in z	EOC	L^1 -error in m	EOC	L^1 -error in n	EOC
20	1.35e-4		1.15890		1.20690	
40	4.28e-5	1.6523	0.36384	1.6714	0.37117	1.7011
80	6.37e-6	2.7500	0.07260	2.3253	0.07506	2.3061
160	8.20e-7	2.9578	0.01339	2.4390	0.01426	2.3958

Table 5: Experimental order of convergence for the second order BDFVLO2 scheme; traveling vortex test.

for all $t \leq t^{n+1}$. By substitution one gets easily

$$\int_0^{2\pi} \sin^m(\theta^1) \cos^n(\theta^1) f(x^1) d\omega = (-1)^{m+n} \int_0^{2\pi} \sin^m(\theta^3) \cos^n(\theta^3) f(x^3) d\omega. \quad (88)$$

Let us define

$$\tilde{v} = \begin{bmatrix} v_1(\mathbf{x}^1) \\ v_2(\mathbf{x}^2) \\ v_3(\mathbf{x}^3) \end{bmatrix} \quad (89)$$

and analogously \tilde{F}, \tilde{S} . Using (37), (39), (43), we get

$$\tilde{F} + \tilde{S} = \begin{bmatrix} \frac{1}{2}\{szD_\theta^+[s] + \sin\theta D_\theta^-[ms] - \cos\theta D_\theta^-[ns]\}(\mathbf{x}^1) \\ -s^2 D_\theta^-[z](\mathbf{x}^2) \\ \frac{1}{2}\{szD_\theta^+[s] - \sin\theta D_\theta^-[ms] + \cos\theta D_\theta^-[ns]\}(\mathbf{x}^3) \end{bmatrix}. \quad (90)$$

Now multiplying (44) by $R(\omega)$ and averaging over 0 to 2π implies

$$w^{n+1}(P) = \frac{1}{2\pi} \int_0^{2\pi} R(\omega) \tilde{v}^n d\omega + \frac{1}{2\pi} \int_0^{2\pi} \int_{t^n}^{t^{n+1}} R(\omega) (\tilde{F} + \tilde{S}) dt d\omega. \quad (91)$$

$$\varepsilon = 0.8, CFL_u = 0.45, CFL \approx 0.9, T = 0.1$$

N	L^1 -error in z	EOC	L^1 -error in m	EOC	L^1 -error in n	EOC
20	0.07541		0.14852		0.14989	
40	0.02770	1.4448	0.03881	1.9363	0.03482	2.1061
80	0.01202	1.2041	0.01430	1.4405	0.00886	1.9746
160	0.00577	1.0602	0.00639	1.1627	0.00285	1.6338

$$\varepsilon = 0.05, CFL_u = 0.45, CFL \approx 7.25, T = 0.1$$

N	L^1 -error in z	EOC	L^1 -error in m	EOC	L^1 -error in n	EOC
20	1.44e-3		0.47355		0.48297	
40	3.39e-4	2.0929	0.11162	2.0849	0.11298	2.0958
80	1.03e-4	1.7218	0.02394	2.2211	0.02382	2.2458
160	4.66e-5	1.1423	0.00708	1.7579	0.00625	1.9306

$$\varepsilon = 0.01, CFL_u = 0.45, CFL \approx 35, T = 0.1$$

N	L^1 -error in z	EOC	L^1 -error in m	EOC	L^1 -error in n	EOC
20	1.37e-4		1.14530		1.17380	
40	4.23e-5	1.6990	0.35955	1.6715	0.35994	1.7053
80	7.10e-6	2.5745	0.07350	2.2904	0.07324	2.2970
160	1.44e-6	2.3019	0.01469	2.3203	0.01438	2.3489

Table 6: Experimental order of convergence for the second order BDFCHARO2 scheme; traveling vortex test.

Remark 7.1 (43) implies that the transformation $\theta \mapsto \theta + \pi$ is equivalent to the following transformations in the first and third components of the integrand in (91):

$$\begin{aligned}
\mathbf{x}^3 &\mapsto \mathbf{x}^1 \\
\sin \omega &\mapsto -\sin \omega \\
\cos \omega &\mapsto -\cos \omega \\
D_{\theta^3}^\pm[f](\mathbf{x}^3) &\mapsto D_{\theta^1}^\pm[f](\mathbf{x}^1).
\end{aligned} \tag{92}$$

Note that for the second bicharacteristic

$$(x^2(t, \omega), y^2(t, \omega), \theta^2(t, \omega)) = (x_P, y_P, \omega). \tag{93}$$

Recall that

$$\int_0^{2\pi} \sin(\omega)^m \cos(\omega)^n d\omega = \begin{cases} 0, & m \text{ or } n \text{ odd} \\ \pi, & m \text{ and } n \text{ even.} \end{cases} \tag{94}$$

Using (92)-(94) we get

$$I_1 := \int_0^{2\pi} R(\omega) \tilde{v}^n d\omega = \int_0^{2\pi} \begin{bmatrix} \frac{sz^n - m^n \cos(\theta) - n^n \sin(\theta)}{s(x_P, y_P)} \\ -\cos(\omega)[sz^n - m^n \cos(\theta) - n^n \sin(\theta)] \\ -\sin(\omega)[sz^n - m^n \cos(\theta) - n^n \sin(\theta)] \end{bmatrix} d\omega + \begin{bmatrix} 0 \\ \pi m^n(x_P, y_P) \\ \pi n^n(x_P, y_P) \end{bmatrix},$$

bottom topography	scheme	RBC	z		q	
			L^1 -error	L^∞ -error	L^1 -error	L^∞ -error
smooth	VLO1	13	$4.1e-14$	$5.3e-14$	$1.1e-13$	$3.6e-13$
smooth	VLO1	11	$2.8e-15$	$3.1e-15$	$2.6e-14$	$8.6e-14$
smooth	VLO1	10	0	0	0	0
discontinuous	VLO1	13	$9.9e-14$	$1.0e-13$	$5.6e-14$	$2.4e-13$
discontinuous	VLO1	11	$6.8e-15$	$7.3e-15$	$4.1e-14$	$2.0e-13$
discontinuous	VLO1	10	0	0	0	0
smooth	BDFVLO2	13	$2.2e-14$	$2.4e-14$	$2.6e-13$	$7.3e-13$
smooth	BDFVLO2	11	$4.8e-15$	$5.3e-15$	$7.3e-14$	$2.6e-13$
smooth	BDFVLO2	10	0	0	0	0
discontinuous	BDFVLO2	13	$2.7e-13$	$2.7e-13$	$1.0e-13$	$5.3e-13$
discontinuous	BDFVLO2	11	$5.6e-14$	$5.7e-14$	$2.5e-14$	$1.2e-13$
discontinuous	BDFVLO2	10	0	0	0	0
smooth	RK2CN	13	$1.0e-14$	$1.4e-14$	$1.3e-13$	$5.1e-13$
smooth	RK2CN	11	$5.8e-15$	$7.2e-15$	$3.5e-14$	$1.2e-13$
discontinuous	RK2CN	13	$1.0e-14$	$1.4e-14$	$1.3e-13$	$5.1e-13$
discontinuous	RK2CN	11	$5.8e-15$	$7.2e-15$	$3.5e-14$	$1.2e-13$

Table 7: Errors between the exact and numerical solution at time $T = 10$ for the lake at rest test with smooth and discontinuous bottom topographies \tilde{b}_s, \tilde{b}_d .

where

$$z^n = z^n(\mathbf{x}^1(t^n, \omega), t^n), \quad m^n = m^n(\mathbf{x}^1(t^n, \omega), t^n), \quad n^n = n^n(\mathbf{x}^1(t^n, \omega), t^n), \\ \theta = \theta^1(t^n, \omega), \quad s = s(\mathbf{x}^1(t^n, \omega)).$$

Further we obtain for the second integral term in (91)

$$I_2 := \int_0^{2\pi} \int_{t^n}^{t^{n+1}} R(\omega)(\tilde{F} + \tilde{S}) dt d\omega \quad (95) \\ = \int_{t^n}^{t^{n+1}} \int_0^{2\pi} \begin{bmatrix} -\frac{1}{s_P} \{szD_\theta^+[s] + \sin(\theta)D_\theta^-[ms] - \cos(\theta)D_\theta^-[ns]\} \\ \cos(\omega) \{szD_\theta^+[s] + \sin(\theta)D_\theta^-[ms] - \cos(\theta)D_\theta^-[ns]\} \\ \sin(\omega) \{szD_\theta^+[s] + \sin(\theta)D_\theta^-[ms] - \cos(\theta)D_\theta^-[ns]\} \end{bmatrix} d\omega dt \\ + s_P^2 \pi \int_{t^n}^{t^{n+1}} \begin{bmatrix} 0 \\ z_x(\mathbf{x}^2, t) \\ z_y(\mathbf{x}^2, t) \end{bmatrix} dt,$$

where

$$z = z(\mathbf{x}^1(t, \omega), t), \quad m = m(\mathbf{x}^1(t, \omega), t), \quad n = n(\mathbf{x}^1(t, \omega), t), \quad \theta = \theta^1(t, \omega), \quad s = s(\mathbf{x}^1(t, \omega)). \quad (96)$$

Finally we get the following evolution operator for $w(P)$:

$$\begin{aligned}
z(P) &= \frac{1}{2\pi s_P} \int_0^{2\pi} \{sz^n - m^n \cos \theta - n^n \sin \theta\} d\omega \\
&\quad - \frac{1}{2\pi s_P} \int_0^{2\pi} \int_{t^n}^{t^{n+1}} \{szD_\theta^+[s] + D_\theta^-[ms] \sin \theta - D_\theta^-[ns] \cos \theta\} dt d\omega
\end{aligned} \tag{97}$$

$$\begin{aligned}
m(P) &= -\frac{1}{2\pi} \int_0^{2\pi} \cos \omega \{sz^n - m^n \cos \theta - n^n \sin \theta\} d\omega \\
&\quad + \frac{1}{2\pi} \int_0^{2\pi} \int_{t^n}^{t^{n+1}} \cos \omega \{szD_\theta^+[s] + D_\theta^-[ms] \sin \theta - D_\theta^-[ns] \cos \theta\} dt d\omega \\
&\quad + \frac{m^n(x_P, y_P)}{2} - \frac{s_P^2}{2} \int_0^{2\pi} z_x(\mathbf{x}^2(t), t) dt
\end{aligned} \tag{98}$$

$$\begin{aligned}
n(P) &= -\frac{1}{2\pi} \int_0^{2\pi} \sin \omega \{sz^n - m^n \cos \theta - n^n \sin \theta\} d\omega \\
&\quad + \frac{1}{2\pi} \int_0^{2\pi} \int_{t^n}^{t^{n+1}} \sin \omega \{szD_\theta^+[s] + D_\theta^-[ms] \sin \theta - D_\theta^-[ns] \cos \theta\} dt d\omega \\
&\quad + \frac{n^n(x_P, y_P)}{2} - \frac{s_P^2}{2} \int_0^{2\pi} z_y(\mathbf{x}^2(t), t) dt.
\end{aligned} \tag{99}$$

Integrating the second and third equation of (34) along the second bicharacteristic from t^n to t^{n+1} leads to

$$\begin{aligned}
m^{n+1}(x_P, y_P) - m^n(x_P, y_P) &= -s_P^2 \int_0^{2\pi} z_x(\mathbf{x}^2(t), t) dt \\
n^{n+1}(x_P, y_P) - n^n(x_P, y_P) &= -s_P^2 \int_0^{2\pi} z_y(\mathbf{x}^2(t), t) dt.
\end{aligned}$$

Plug in the last expressions in the equations (98), (99) for $m(P), n(P)$ we obtain the exact integral representation (45) - (47)

$$\begin{aligned}
z(P) &= \frac{1}{2\pi s_P} \int_0^{2\pi} \{sz^n - m^n \cos \theta - n^n \sin \theta\} d\omega \\
&\quad - \frac{1}{2\pi s_P} \int_0^{2\pi} \int_{t^n}^{t^{n+1}} \{szD_\theta^+[s] + D_\theta^-[ms] \sin \theta - D_\theta^-[ns] \cos \theta\} dt d\omega
\end{aligned} \tag{45}$$

$$\begin{aligned}
m(P) &= -\frac{1}{\pi} \int_0^{2\pi} \cos \omega \{sz^n - m^n \cos \theta - n^n \sin \theta\} d\omega \\
&\quad + \frac{1}{\pi} \int_0^{2\pi} \int_{t^n}^{t^{n+1}} \cos \omega \{szD_\theta^+[s] + D_\theta^-[ms] \sin \theta - D_\theta^-[ns] \cos \theta\} dt d\omega
\end{aligned} \tag{46}$$

$$\begin{aligned}
n(P) &= -\frac{1}{\pi} \int_0^{2\pi} \sin \omega \{sz^n - m^n \cos \theta - n^n \sin \theta\} d\omega \\
&\quad + \frac{1}{\pi} \int_0^{2\pi} \int_{t^n}^{t^{n+1}} \sin \omega \{szD_\theta^+[s] + D_\theta^-[ms] \sin \theta - D_\theta^-[ns] \cos \theta\} dt d\omega.
\end{aligned} \tag{47}$$

Note that we use here the same numbering of the exact integral representation as in Section 3.

Acknowledgements: This work has been partially supported by the German Science Foundation under the grants LU 1470/2-2 and No 361/3-2. The second author has been supported by the Alexander-von-Humboldt Foundation through a postdoctoral fellowship. M.L. and G.B. would like to thank Dr. Leonid Yelash (JGU Mainz) for fruitful discussions.

References

- [1] K.R. Arun, M. Kraft, M. Lukáčová-Medvid'ová, and Ph. Prasad. Finite volume evolution Galerkin method for hyperbolic conservation laws with spatially varying flux functions. *J. Comput. Phys.*, 228:565–590, 2009.
- [2] K.R. Arun and S. Noelle. An asymptotic preserving scheme for low Froude number shallow flows. *accepted to the Proceedings of the 14th International Conference on Hyperbolic Problems. Theory, Numerics and Applications, American Institute of Mathematical Sciences*, 2013.
- [3] K.R. Arun, S. Noelle, M. Lukáčová Medvid'ová, and C.-D. Munz. Asymptotic preserving all Mach number scheme for the Euler equations of gas dynamics. *submitted to SIAM J. Sci. Comput.* 2012.
- [4] E. Audusse, F. Bouchut, M. Bristeau, R. Klein, and B. Perthame. A fast and stable well-balanced scheme with hydrostatic reconstruction for shallow water flows. *SIAM J. Sci. Comput.*, 25(6):2050–2065, 2004.
- [5] A. Bermúdez and M.E. Vázquez. Upwind methods for hyperbolic conservation laws with source terms. *Comput. Fluids*, 23(8):1049–1071, 1994.
- [6] H. Bijl and P. Wesseling. A unified method for computing incompressible and compressible flows in boundary-fitted coordinates. *J. Comput. Phys.*, 141(2):153–173, 1998.

- [7] N. Botta, R. Klein, S. Langenberg, and S. Lützenkirchen. Well balanced finite volume methods for nearly hydrostatic flows. *J. Comput. Phys.*, 196(2):539–565, 2004.
- [8] F. Bouchut, J. Le Sommer, and V. Zeitlin. Frontal geostrophic adjustment and non-linear wave phenomena in one-dimensional rotating shallow water. II: High-resolution numerical simulations. *J. Fluid Mech.*, 514:35–63, 2004.
- [9] D. Bresch, R. Klein, and C. Lucas. Multiscale analyses for the shallow water equations. *Computational Science and High Performance Computing IV, Notes on Numerical Fluid Mechanics and Multidisciplinary Design* 115, 149–164, 2011.
- [10] A. Canestrelli, M. Dumbser, A. Siviglia, and E.F. Toro. Well-balanced high-order centered schemes on unstructured meshes for shallow water equations with fixed and mobile bed. *Advanced in Water Resources*, 33:291–303, 2010.
- [11] Manuel J. Castro Díaz, J. M. González-Vida, Jorge Macías, and Carlos Parés. Realistic application of a tidal 2D two-layer shallow water model to the Strait of Gibraltar. *AIP Conf. Proceedings* 168, 1429–1432, 2009.
- [12] P. Degond and M. Tang. All speed scheme for the low Mach number limit of the isentropic Euler equations. *Commun. Comput. Phys.*, 10:1–31, 2011.
- [13] M. Feistauer, J. Felcman, and I. Straškraba. *Mathematical and Computational Methods for Compressible Flow*. Oxford University Press, 2003.
- [14] F.X. Giraldo and M. Restelli. High-order semi-implicit time-integrators for a triangular discontinuous Galerkin oceanic shallow water model. *Int. J. Numer. Methods Fluids*, 63(9):1077–1102, 2010.
- [15] F.X. Giraldo, M. Restelli, and M. Läuter. Semi-implicit formulations of the Navier-Stokes equations: application to nonhydrostatic atmospheric modeling. *J. Sci. Comput.*, 32(6):3394–3425, 2010.
- [16] J.M. Greenberg and A.-Y. Le Roux. A well-balanced scheme for the numerical processing of source terms in hyperbolic equations. *SIAM J. Numer. Anal.*, 33(1):1–16, 1996.
- [17] J. Haack, S. Jin, and J. Liu. An all-speed asymptotic-preserving method for the isentropic Euler and Navier-Stokes equations. *Commun. Comput. Phys.*, 12:955–980, 2012.
- [18] L. B. Hoffmann. *Ein zeitlich selbstadaptives numerisches Verfahren zur berechnung von Strömungen aller Mach-Zahlen basierend auf Mehrskalenasymptotik und diskreter Datenanalys*. PhD thesis, Universität Hamburg, 2000.
- [19] S. Jin. Efficient asymptotic-preserving (AP) schemes for some multiscale kinetic equations. *SIAM J. Sci. Comput.*, 21(2):441–454, 1999.
- [20] S. Klainerman and A. Majda. Singular limits of quasilinear hyperbolic systems with large parameters and the incompressible limit of compressible fluids. *Commun. Pure Appl. Math.*, 34:481–524, 1981.

- [21] R. Klein, N. Botta, T. Schneider, C.-D. Munz, S. Roller, A. Meister, L. Hoffmann, and T. Sonar. Asymptotic adaptive methods for multi-scale problems in fluid mechanics. *J. Eng. Math.*, 39(1-4):261–343, 2001.
- [22] R. Klein. An applied mathematical view of meteorological modelling. Hill, James M. et al. (eds.), *Applied mathematics entering the 21st century, Proceedings in Applied Mathematics* 116:227–269, 2004.
- [23] J.B. Klemp, W.C. Skamarock, and J. Dudhia. Conservative split-explicit time integration methods for the compressible nonhydrostatic equations. *Monthly Weather Rev.*, 135:2897–2913, 2007.
- [24] A. Kurganov and D. Levy. Central-upwind schemes for the Saint-Venant system. *Math. Model. Numer. Anal.*, 36(3):397–425, 2002.
- [25] R.J. LeVeque. Balancing source terms and flux gradients in high-resolution Godunov methods: The quasi-steady wave-propagation algorithm. *J. Comput. Phys.*, 146(1):346–365, 1998.
- [26] Q. Liang, A.G.L. Borthwick. Adaptive quadtree simulation of shallow flows with wet-dry fronts over complex topography. *Comput. Fluids*, 38(2):221–234, 2009.
- [27] Q. Liang, F. Marche. Numerical resolution of well-balanced shallow water equations with complex source terms. *Adv. Water Resour.*, 32(6): 873-884, 2009.
- [28] M. Lukáčová-Medvidová, K.W. Morton, and G. Warnecke. Finite volume evolution Galerkin methods for hyperbolic systems. *J. Sci. Comput.*, 26(1):1–30, 2004.
- [29] M. Lukáčová-Medvidová, K.W. Morton, and Gerald Warnecke. Evolution Galerkin methods for hyperbolic systems in two space dimensions. *Math. Comput.*, 69(232):1355–1384, 2000.
- [30] M. Lukáčová Medvidová, A. Müller, V. Wirth, and L. Yelash. Large time step discontinuous evolution Galerkin methods for multiscale atmospheric flow. *submitted to J. Comput. Phys.*, 2013.
- [31] M. Lukáčová-Medvidová and K.W. Morton. Finite volume evolution Galerkin methods – A survey. *Indian J. Pure Appl. Math.*, 41(2):329–361, 2010.
- [32] M. Lukáčová-Medvidová, S. Noelle, and M. Kraft. Well-balanced finite volume evolution Galerkin methods for the shallow water equations. *J. Comput. Phys.*, 221(1):122–147, 2007.
- [33] A. Majda. *Introduction to PDEs and Waves for the Atmosphere and Ocean*, Lecture Notes, Courant Institute, 2003.
- [34] A. Müller, J. Behrens, F.X. Giraldo, and V. Wirth. Comparison between adaptive and uniform discontinuous Galerkin simulations in dry 2d bubble experiments. *J. Comput. Phys.*, 235:371–393, 2013.
- [35] C.-D. Munz, S. Roller, R. Klein, and K.J. Geratz. The extension of incompressible flow solvers to the weakly compressible regime. *Comput. Fluids*, 32(2):173–196, 2003.

- [36] J.H. Park and C.-D. Munz. Multiple pressure variables methods for fluid flow at all Mach numbers. *Int. J. Numer. Methods Fluids*, 49(8):905–931, 2005.
- [37] P. Prasad. Ray theories for hyperbolic waves, kinematical conservation laws (KCL) and applications. *Indian J. Pure Appl. Math.*, 38(5):467–490, 2007.
- [38] M. Restelli. *Semi-Lagrangian and Semi-Implicit Discontinuous Galerkin Methods for Atmospheric Modeling Applications*. PhD thesis, Politecnico di Milano, 2007.
- [39] M. Restelli and F.X. Giraldo. A conservative discontinuous Galerkin semi-implicit formulation for the Navier-Stokes equations in nonhydrostatic mesoscale modeling. *SIAM J. Sci. Comput.*, 31(3):2231–2257, 2009.
- [40] M. Ricchiuto and A. Bollermann. Stabilized residual distribution for shallow water simulations. *J. Comput. Phys.*, 228(4):1071–1115, 2009.
- [41] B. Rogers, A.G.L. Borthwick, and P.H. Taylor. Mathematical balancing of flux gradient and source terms prior to using Roe’s approximate Riemann solver. *J. Comput. Phys.*, 192(2):422–451, 2003.
- [42] B. Rogers, M. Fujihara, and A.G.L. Borthwick. Adaptive Q-tree Godunov-type scheme for shallow water equations. *Int. J. Numer. Methods Fluids*, 35(3):247–280, 2001.
- [43] Y. Sun and Y. Ren. The finite volume local evolution Galerkin method for solving the hyperbolic conservation laws. *J. Comput. Phys.*, 228(13):4945–4960, 2009.
- [44] G. Stecca, A. Siviglia and E. F. Toro. A finite volume upwind-biased centred scheme for hyperbolic systems of conservation laws. Application to shallow water equations. *Commun. Comput. Phys.*, 12(4):1183–1214, 2012.
- [45] G.K. Vallis. *Atmospheric and Oceanic Fluid Dynamics*. Cambridge University Press, 2006.

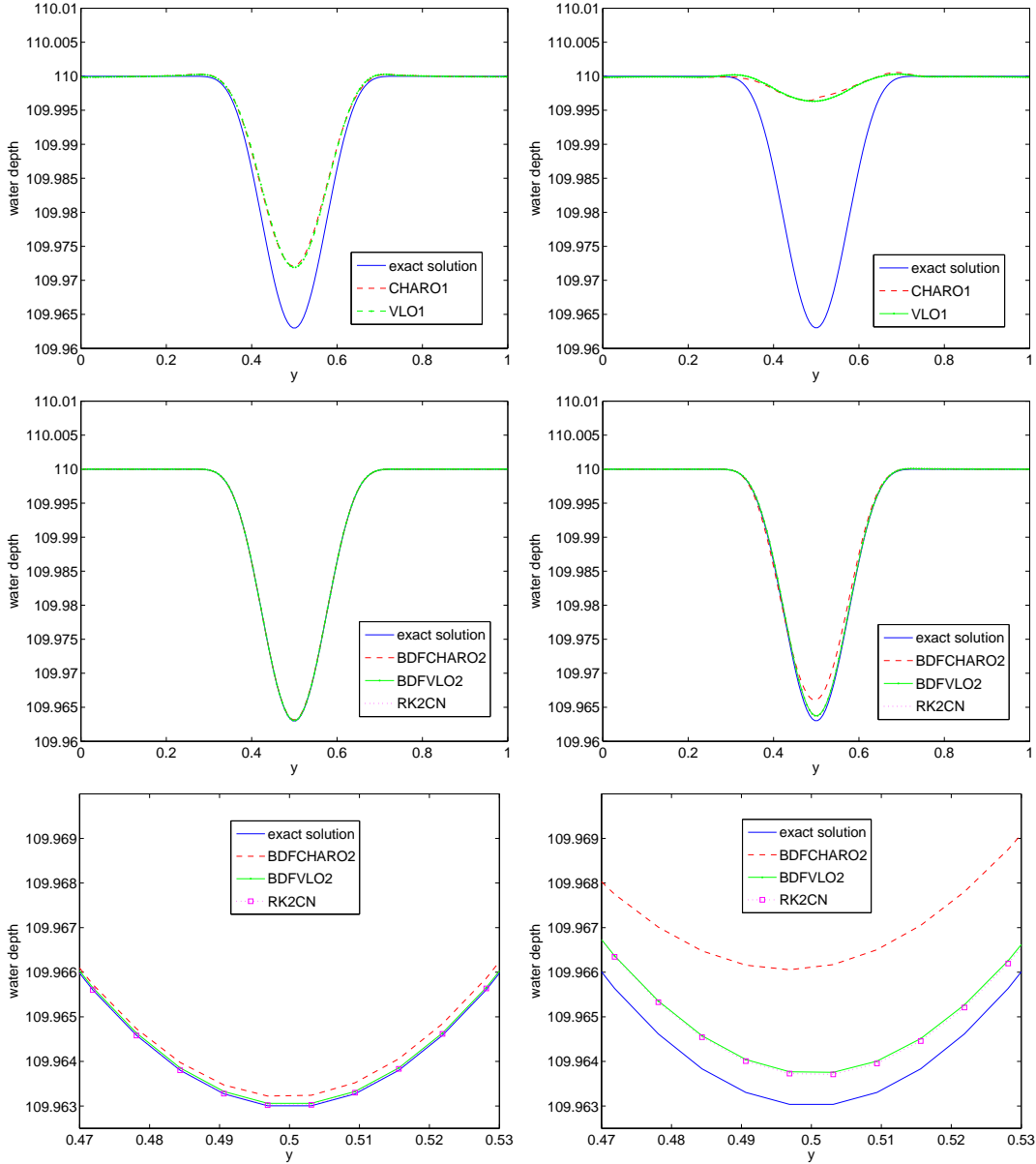


Figure 4: Cuts of numerical solutions of the traveling vortex experiment with Froude number $\varepsilon = 0.05$ at $x = 0.56, T = 0.1$ on the left and $x = 0.5, T = 5/3$ on the right. In the first row results obtained by the first order schemes CHARO1, VLO1 are depicted. The second order schemes BDFCHARO2, BDFVLO2 and RK2CN are presented in the middle and last row (zoomed solution). A mesh with 160×160 cells was used.

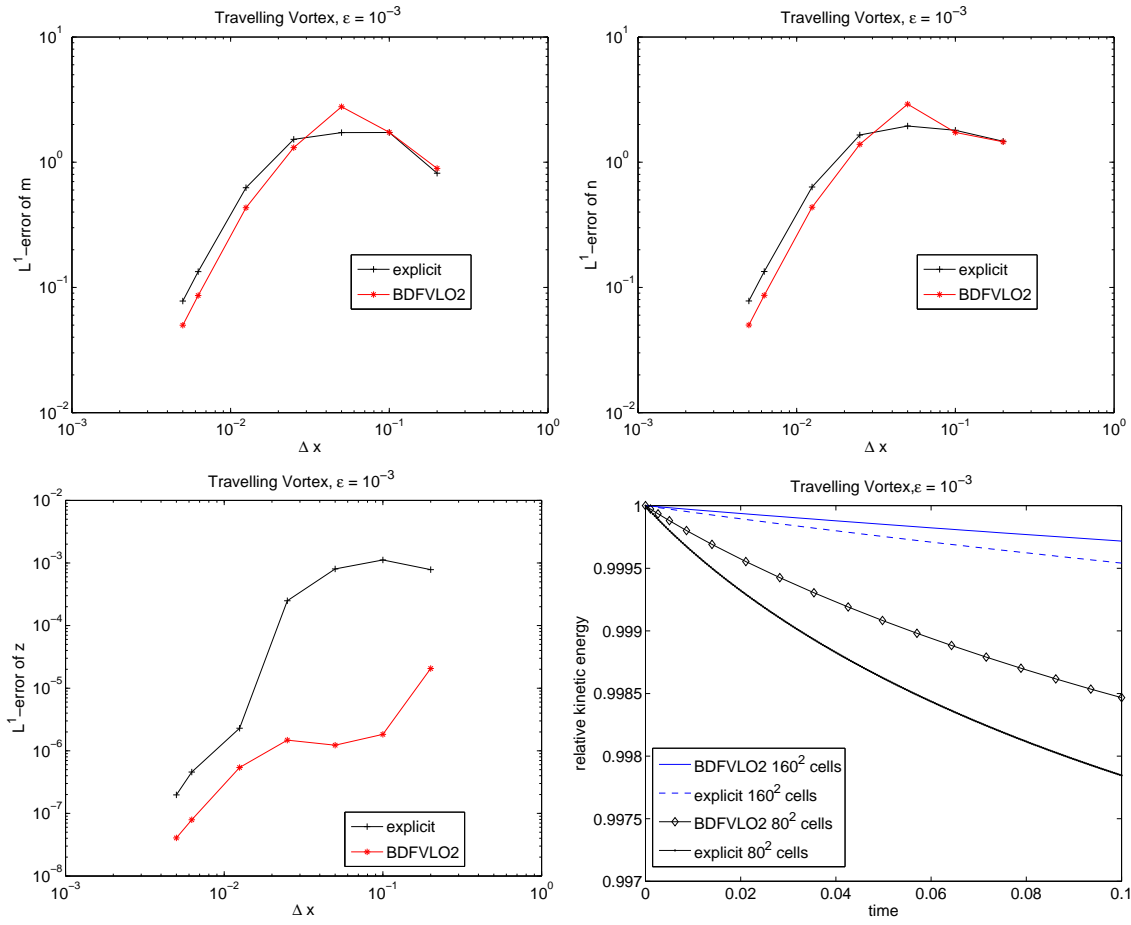


Figure 5: Comparison of the L^1 - errors of the explicit FVEG scheme [32] and the large time step IMEX-type BDFVLO2 scheme for travelling vortex experiment with $\epsilon = 0.001$ and different mesh resolutions $\Delta x = 5, 10, 20, 40, 80, 160$. The relative kinetic energy (bottom right) is computed on two meshes with 80×80 and 160×160 cells.

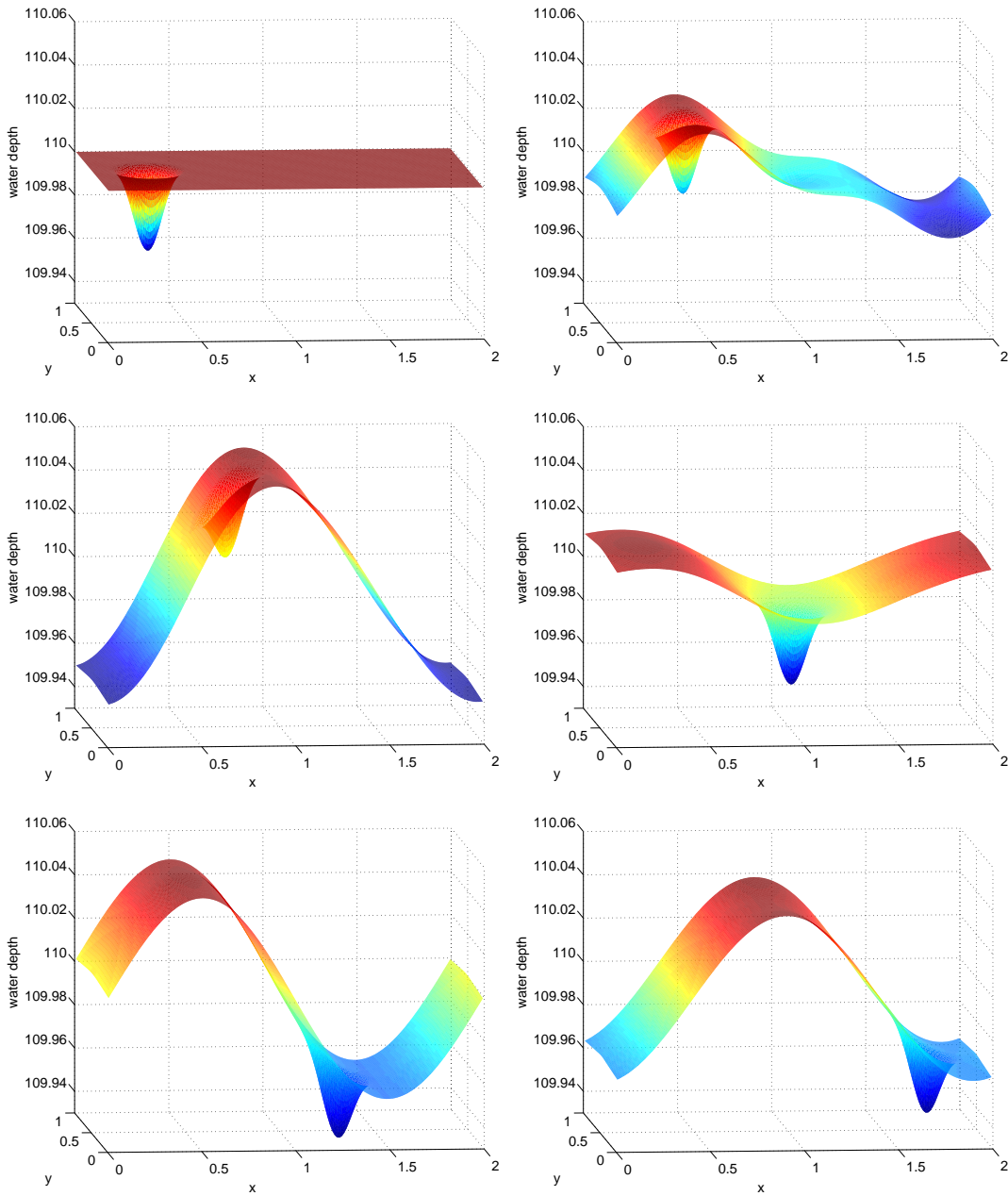


Figure 6: Time evolution of the water depth for the travelling vortex test with non-constant bottom topography, the Froude number $\varepsilon = 0.05$, time instants are (from left to right and from top to bottom) $T = 0, 0.24, 0.71, 1.18, 1.65, 2.35$.

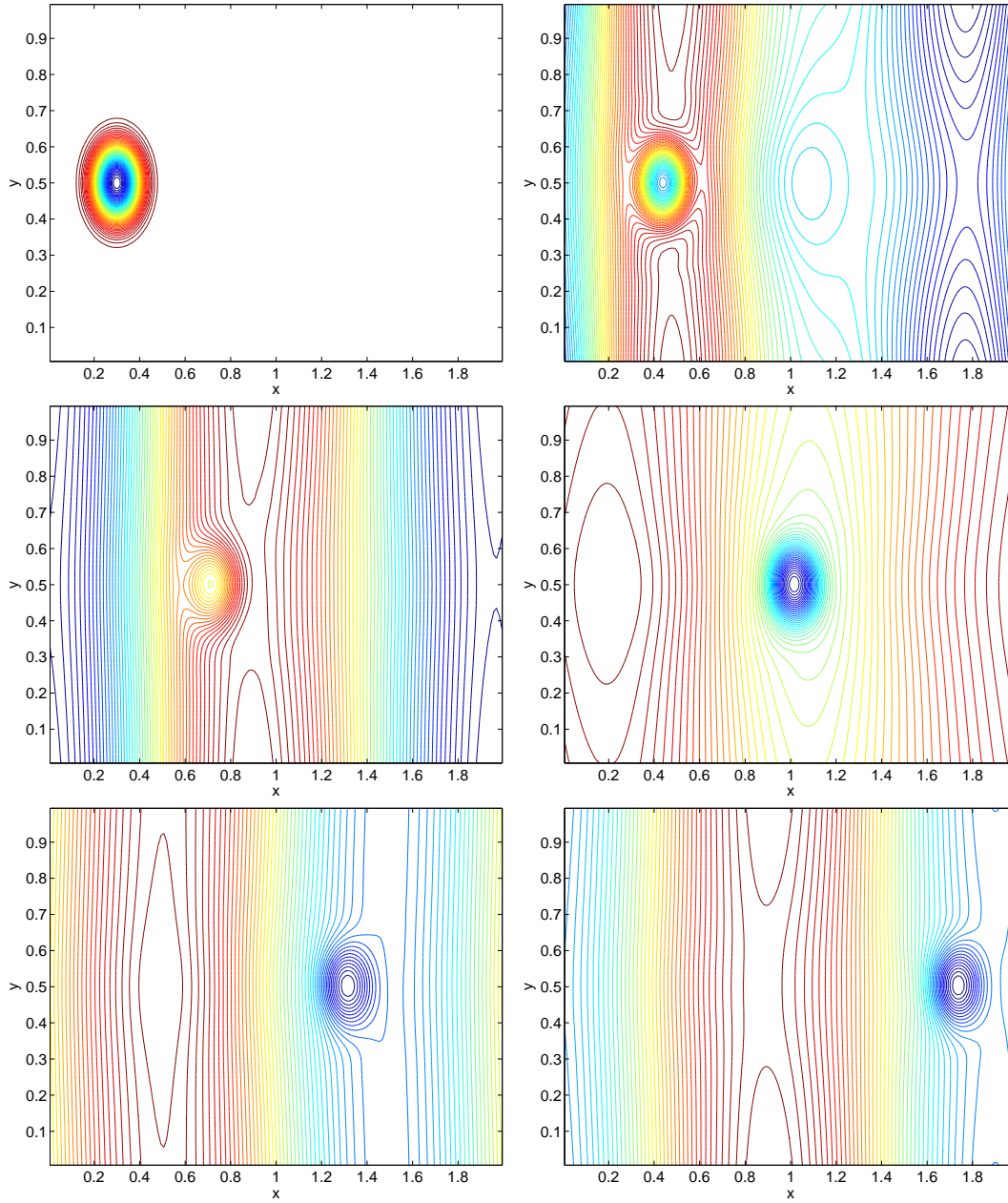


Figure 7: Isolines for the water depth for the travelling vortex test with non-constant bottom topography, the Froude number $\varepsilon = 0.05$, time instants are (from left to right and from top to bottom) $T = 0, 0.24, 0.71, 1.18, 1.65, 2.35$.

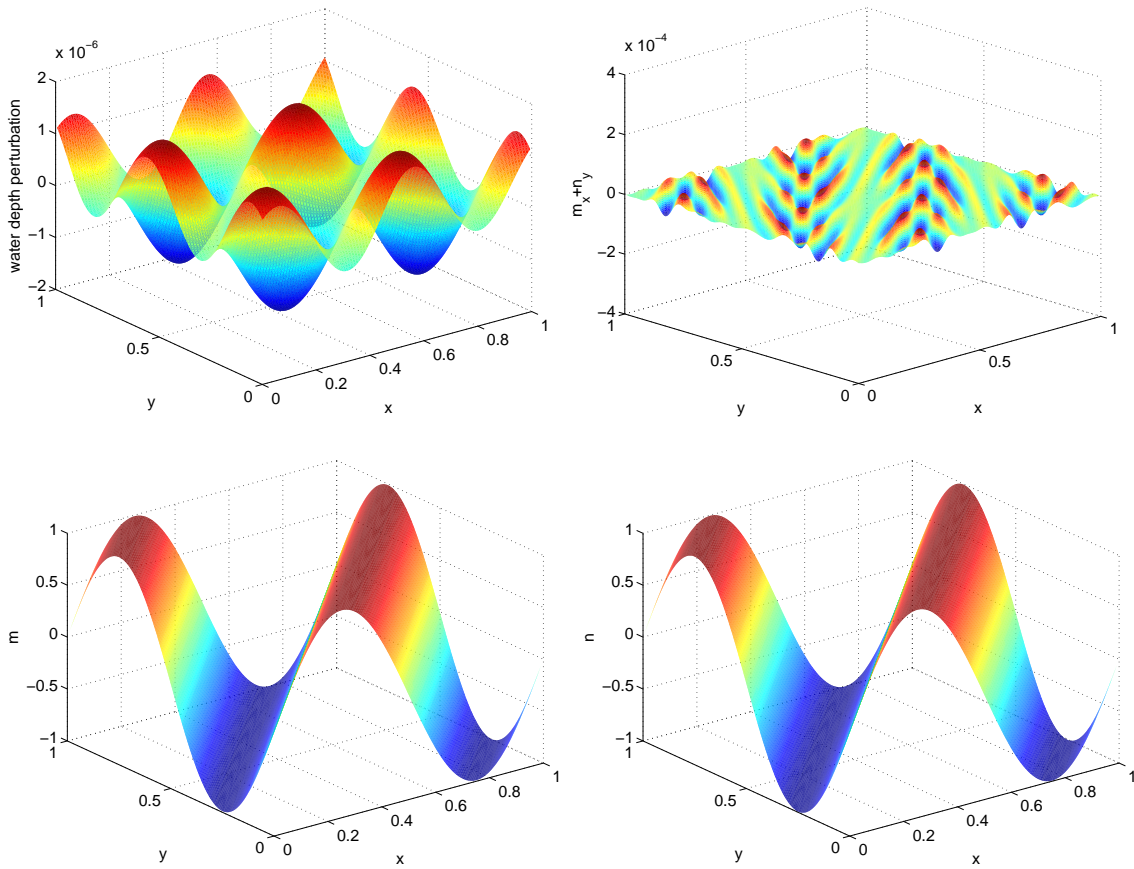


Figure 8: Numerical solution of the sine wave example with $\varepsilon = 0.05$ at time $T = 1$. The pictures show (from top to bottom and left to right): water depth perturbation of $RBC = 1.00125$, divergence of momentum, first and second component of momentum.

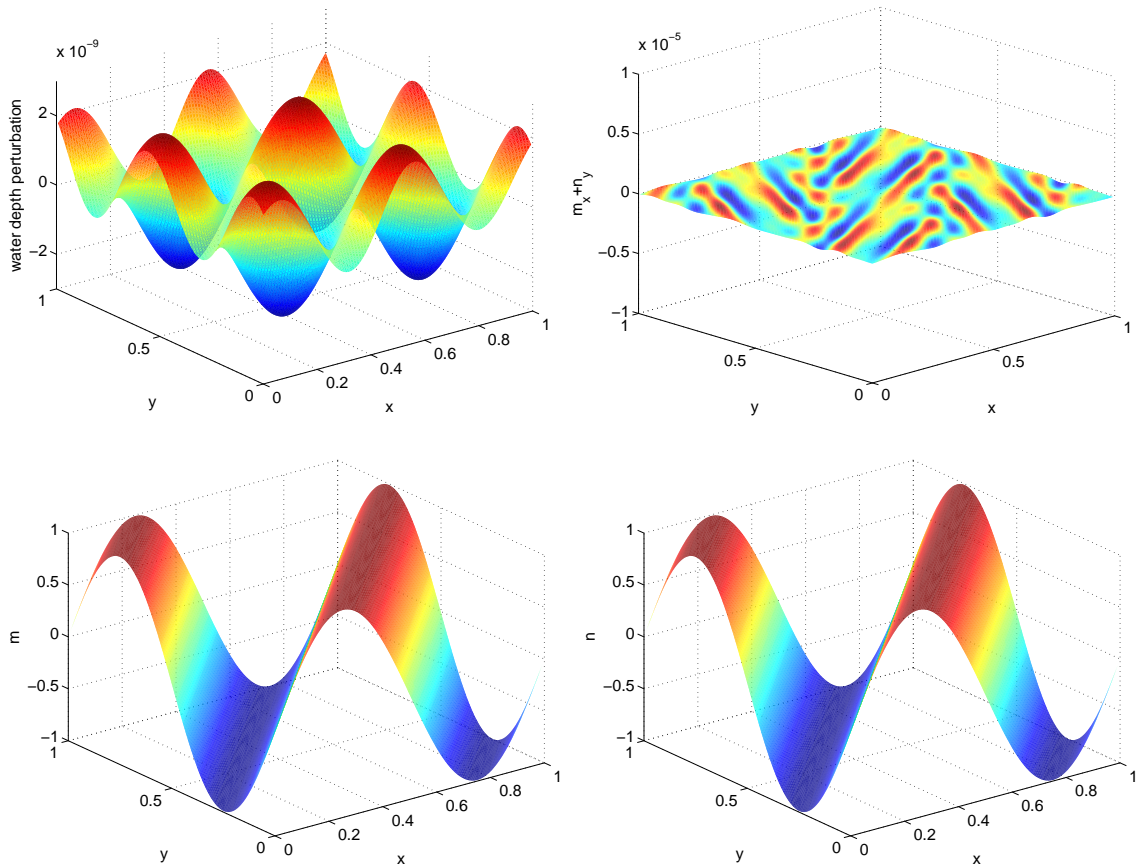


Figure 9: Numerical solution of the sine wave example with Froude number $\varepsilon = 0.01$ at time $T = 1$. The pictures show (from top to bottom and left to right): water depth perturbation of $RBC = 1.00005$, divergence of momentum, first and second component of momentum.